Persistent Anomalies, Blocking and Variations in Atmospheric Predictability[1]

B. LEGRAS

Laboratoire de Météorologie Dynamique, ENS/CNRS, 75231 Paris Cedex 05, France

M. GHIL

Courant Institute of Mathematical Sciences, New York University, New York, NY 10012 and Department of Atmospheric Sciences and Institute of Geophysics and Planetary Physics, University of California, Los Angeles, CA 90024

(Manuscript received 16 July 1984, in final form 13 November 1984)

ABSTRACT

We consider regimes of low-frequency variability in large-scale atmospheric dynamics. The model used for the study of these regimes is the fully-nonlinear, equivalent-barotropic vorticity equation on the sphere, with simplified forcing, dissipation and topography. Twenty-five modes are retained in a spherical harmonics expansion of the streamfunction. Solutions are studied as a function of the nondimensional intensity of the forcing and dissipation.

Multiple stationary solutions are obtained as a result of nonlinear interaction between waves, mean flow and orography. The number of modes retained in the analysis permits these multiple equilibria to appear for realistic values of the forcing. The equilibria exhibit blocked and zonal flow patterns bearing a marked resemblance to synoptically defined zonal and blocked Northern Hemisphere midlatitude flows.

Wave–wave interactions influence strongly the stability properties of the equilibria and the time evolution of nonequilibrium solutions. Time-dependent solutions show persistent sequences which occur in the phase-space vicinity of the zonal and blocked equilibria. Composite flow patterns of the persistent sequences are similar to the equilibria nearby, which permits the unambiguous definition of quasi-stationary flow regimes, zonal and blocked, respectively. The number of episodes of blocked or zonal flow decreases monotonically as their duration increases, in agreement with observations.

The statistics of transitions between the two types of planetary flow regimes are computed from the model's deterministic dynamics. These transitions, called breaks in statistical-synoptic long-range forecasting, are shown to be influenced by changes in model parameters. This influence is discussed in terms of the effect of anomalous boundary conditions on large-scale midlatitude atmospheric flow and on its predictability.

1. Introduction

The global atmosphere is probably the fluid system for which the most detailed sets of observations are available on a routine basis. In many fluid systems on the laboratory and industrial scale, it suffices to know, describe and explain the *mean state* of the system and perhaps the statistics of its *fluctuations*. In the atmosphere, an individual fluctuation is a cyclone or hurricane which may affect the life and well-being of millions. Observing and understanding such a fluctuation is therefore of great importance.

The success of baroclinic instability theory (Charney, 1947; Eady, 1949) in explaining many features of extratropical cyclones has led to a flourishing of meteorological literature concerned with elaborating the details of the theory. The development of this classical theory has proceeded, however, in two separate directions: the study of the individual growth and life cycle of the most important fluctuations (Pedlosky, 1979, Ch. 7) on the one hand, and the contribution of the ensemble of these fluctuations to the maintenance of the mean flow (Lorenz, 1967) on the other.

The dual character of meteorological research suggested above was accompanied by a natural tendency to consider mathematically the individual fluctuations as unstably growing *perturbations on a mean flow*. This flow is usually taken as steady and zonal, i.e., as parallel to circles of latitude. In reality, the observed finite-time average atmospheric flow is neither truly steady, nor zonal, nor is it a solution of the full, nonlinear equations of motion. These facts have not prevented the already mentioned successes in studying certain types of short-term atmospheric fluctuations as solutions to the flow equations linearized about a steady mean zonal state.

Recently, attention has turned again to the fact that deviations from a climatological mean state occur that have life spans of weeks to months (Namias,

[1] Partial results of our investigation were reported at the Third and Fourth Conferences on Atmospheric and Oceanic Waves and Stability of the American Meteorological Society, held in San Diego, January 1981, and in Boston, March 1983, and at other scientific and professional meetings during this period.

1982; Rasmusson and Wallace, 1983), and thus exceed considerably the average life span of cyclones, of three to five days. Some of these *persistent anomalies,* moreover, have a recognizable quasi-stationary spatial pattern and a statistical distribution of life span which is exponential in character, like that for rapidly propagating cyclones, but is numerically distinct from the tail of the latter distribution (Dole and Gordon, 1983).

Among persistent anomalies, the *blocking* pattern, as documented by Rex (1950a,b), consists in the appearance of a quasi-stationary center of high pressure, located at about 50°N in certain preferred areas, off the western margins of the continents. This blocking high may persist for longer than ten days. It deflects the traveling cyclones from the usual storm tracks and produces a strong southward advection of polar air on its eastern flank, inducing severe cold episodes in winter. The occurrence or the nonoccurrence of this feature determines to a large extent the distinctive character of an individual season; it is therefore of great importance to weekly and monthly mean weather prediction.

During the 1950s, very limited progress was made in providing a theoretical explanation of blocking, and no consensus was reached among synoptic meteorologists concerning its definition and description. The problem attracted little attention in the 1960s and early 1970s, while progress in other parts of the field was rapid.

In the late 1970s, the economic impact of a number of blocking episodes, together with the availability of extensive observations and of new theoretical and computational tools, brought a renewed interest in the topic. The onset of certain persistent anomalies, like the initial growth of cyclones, could be explained now by more sophisticated *linear wave theories.* Resonant forcing of stationary Rossby waves by topography (Tung and Lindzen, 1979) or propagation of wave trains produced by tropical sea surface temperature anomalies (SSTAs) into midlatitudes (Hoskins and Karoly, 1981) were able to produce the strong zonal asymmetries of flow associated with some quasi-stationary, persistent anomalies. The problem with the linear approach is that the duration of atmospheric anomalous events is often shorter than that of SSTAs and much shorter than that of topographic features. The duration of atmospheric anomalies depends moreover on the persistence of the mean flow itself, which is undetermined in the linear approach.

Egger (1978) was the first to suggest that internal atmospheric variability, modeled by nonlinear wave–wave interactions, could account for the finite amplitude and duration of blocking events. Charney and DeVore (1979) took the more general view that blocking and near-zonal flow could be associated with two distinct, stable stationary solutions of a quasi-linear, spectrally truncated barotropic vorticity equation governing the flow. Transitions between these two preferred regimes might occur in the atmosphere as the result of fluctuations not explicitly modeled in their system. Similar results were obtained with different methods by Pedlosky (1981), who also studied a baroclinic extension of the model. Finite, exponentially-distributed residence times for two distinct nonstationary regimes appear in the fully nonlinear baroclinic model of Reinhold and Pierrehumbert (1982).

The purpose of the present article is to attempt a description of large-scale atmospheric flow in terms of *multiple regimes,* each of which has a characteristic spatial pattern and a characteristic mean residence time. An important objective of this approach is to associate the characteristic length of the exponentially-distributed residence times for each regime with its predictability in an operational weather forecasting model, whether numerical, statistical or hybrid.

The model studied in this paper is governed by the equivalent-barotropic form of the potential vorticity equation on the sphere, with simplified topography, a forced midlatitude zonal jet, and Ekman dissipation. In Section 2 we describe the model, which has certain similarities with that of Källén (1984), and its discretization into 25 spherical harmonics, with 132 nonlinear triad interactions among them.

In Section 3 we present the stationary solutions, and their dependence on the model's two main nondimensional parameters: the Rossby number of the forcing, and the dissipation coefficient. Multiple equilibria for the same parameter values and two types of nonlinear resonance are obtained. Some results on how equilibrium solutions change with the modeled topographic height are also included. The relative realism of some of the spatial patterns of these solutions, blocked and nearly-zonal, is striking for such a simple model.

This realism suggests that our simple model, used here mainly for illustrative, methodological purposes, might have some relevance to the actual behavior of large-scale midlatitude atmospheric flow. The spatial structure of this flow's low frequency part is known indeed to be to a large extent barotropic (Blackmon *et al.,* 1979; N.-C. Lau, personal communication, 1983), although some of the mechanisms leading to the maintenance of this structure, or to changes in it, are probably baroclinic (Itoh, 1985).

In Section 4 we investigate the stability of the stationary solutions, most of which are unstable for realistic parameter values. The transition to periodic and aperiodic solution behavior is outlined briefly.

The article's main results are contained in Section 5. The persistence of aperiodic solutions near certain unstable equilibria is studied in detail.

The time-mean flow pattern during the persistent episodes is shown to resemble closely the neighboring equilibrium pattern, whether nearly-zonal or blocked.

The persistence times are distributed almost exponentially with characteristic decay time depending on the regime and on external parameters. These times are typically longer than those obtained by Dole and Gordon (1983) from observations, presumably due to the limited resolution and to the absence of baroclinic, short-lived fluctuations from the model.

The algebraically largest eigenvalue of the model equation's right-hand side, linearized about the instantaneous position of the solution in its phase space, is computed as a function of time. This eigenvalue's sign and size are correlated in certain cases with the persistent episodes, thus providing some hope of obtaining an *a priori* measure of a flow pattern's predictability in operational models.

The results are discussed in Section 6, and compared with observations on the variability of the atmosphere's general circulation. A number of extensions and applications of the present approach are outlined.

Two appendices provide details on the analytic and numerical methods for studying stationary solutions of a model with a relatively large number of degrees of freedom. A third appendix analyzes the behavior of linear resonances when the meridional structure of the flow becomes more complicated, as it is in our second nonlinear resonance.

2. Model description

The model is governed by the equivalent-barotropic form of the equation for the *conservation of potential vorticity* (Charney, 1973, Sec. 6; Pedlosky, 1979, Sec. 3.12) on the sphere:

$$\frac{\partial}{\partial t}(\Delta - L_R^{-2})\psi + J\left[\psi, \Delta\psi + f\left(1 + \frac{h}{H}\right)\right] = \alpha\Delta(\psi^* - \psi). \quad (1)$$

Here ψ is the streamfunction, Δ the horizontal Laplacian, J the Jacobian operator, f the Coriolis parameter, h the topographic height and H the scale height of the atmosphere. The right-hand side induces a relaxation towards the forcing streamfunction ψ^* with a characteristic time α^{-1}. The external radius of deformation is L_R; it represents to first order the effects of compressibility associated with small displacements of the equivalent free surface.

In spherical geometry, the natural horizontal coordinates are the longitude ϕ and the sine of the latitude $\mu = \sin\theta$. All variables are scaled by the radius of the earth a, its angular velocity Ω and a characteristic speed U, yielding the nondimensional variables

$$L_R = a\lambda, \quad h = Hh', \quad t = t'/2\Omega; \quad (2a,b,c)$$

$$(\psi, \psi^*) = aU(\psi', \psi^{*\prime}), \quad \alpha = 2\Omega\alpha', f = 2\Omega\mu. \quad (2d,e,f,g)$$

The nondimensional form of the equation, dropping the primes, is thus given by:

$$\frac{\partial}{\partial t}(\Delta - \lambda^{-2})\psi + \rho J(\psi, \Delta\psi) + J[\psi, \mu(1 + h)] = \alpha\Delta(\psi^* - \psi), \quad (3)$$

where the nondimensional number $\rho = U/2\Omega a$ is similar to a Rossby number and measures the intensity of the forcing, cf. (2e). It multiplies [cf. (2d)] the sole nonlinear term in (3) and, as we shall see, plays the role of a critical parameter for the behavior of the solutions. We note that the use of the same scaling for ψ and ψ^*, Eqs. (2d, e), is consistent and is also justified *a posteriori* by the fact that the energy of the response ψ is always of the same order as or smaller than that of the forcing ψ^*, for stationary as well as for time-dependent solutions.

Equation (3) is discretized through a truncated expansion is spherical harmonics $Y_l^m(\phi, \mu) = P_l^m(\mu) \times e^{im\phi}$,

$$\psi(\phi, \mu, t) = \sum_{l=0}^{L} \sum_{m=-l}^{l} \psi_l^m(t) Y_l^m(\phi, \mu), \quad (4)$$

where $P_l^m(\mu)$ are associated Legendre functions, and $L = 9$. We assume equatorial symmetry of the flow, as well as a sectorial periodicity (mod π) in longitude. The resulting $N = (L + 1)^2/4 = 25$ real modes are circled in Fig. 1. They allow 132 triadic nonlinear interactions. Each triad conserves energy and potential

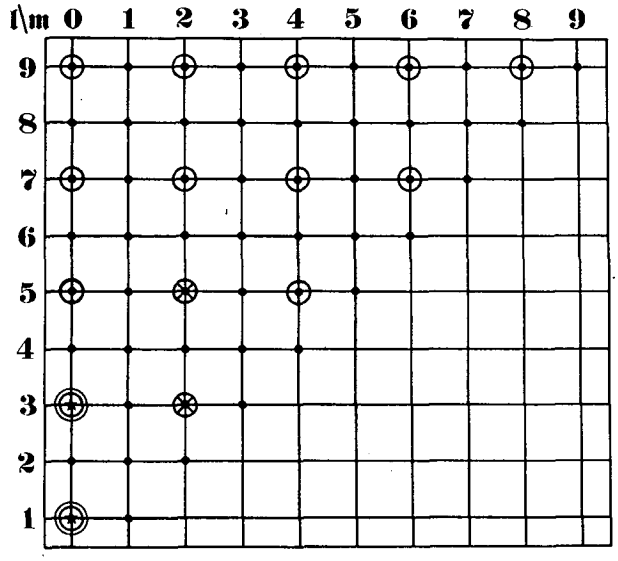

FIG. 1. Spectral truncation of the model, Eqs. (1)–(7), in spherical harmonics: m is the zonal and l the total wavenumber. Modes retained in the flow fields ψ are circled. Topographic modes are crossed and forcing zonal modes are indicated by a double circle. Note symmetry about equator implied by $l + m$ odd and invariance under rotation by 180° longitude implied by m even.

enstrophy, and so does the whole truncated system in the absence of forcing and dissipation. In particular, the topography acts solely as a catalyst transferring the energy between different scales.

The topography (Fig. 2) is depicted as the most coarse representation of the Northern Hemisphere, with two equal continental masses separated by two equal oceans:

$$h = 4h_0\mu^2(1 - \mu^2)\cos 2\phi. \tag{5a}$$

The multiplication of h by the nondimensional Coriolis parameter μ leads to the term μh consisting of the modes marked by a cross in Fig. 1. We shall use $h_0 = 0.1$, except in connection with the series of results reported in Fig. 4 and further analyzed in Appendix C.

The topographic contour map in Fig. 2 and all subsequent maps of the stream function $\psi = \psi(\phi, \mu)$ use a conformal conical projection of ratio 2/3 (Cotter, 1966, Ch. 8). This projection maps a sector of the Northern Hemisphere located between 0° and 270° longitude onto the half disk shown in the figure. The advantage is that one-half of the continent and one-half of the ocean are repeated, making the two-periodic pattern easier to perceive, without requiring the additional space that would be taken up by the full disk.

The mean forcing is a zonal jet, expanded in the first two zonal components marked with a double circle in Fig. 1,

$$\psi^* = -\kappa\mu^3 = aY_1^0(\mu) + bY_3^0(\mu); \tag{5b}$$

κ is a nondimensional constant chosen so that the maximum forcing speed, which occurs at 50°N, has a dimensional value of 60 m s^{-1} for $\rho = 0.20$.

The truncation above allows an exact representation of the direct interaction between the forcing and the orography. The forcing ψ^* models, in the absence of explicit baroclinic effects, the mean thermal wind which would be observed in the case of an idealized purely zonal circulation, with no meridional mass transfer.

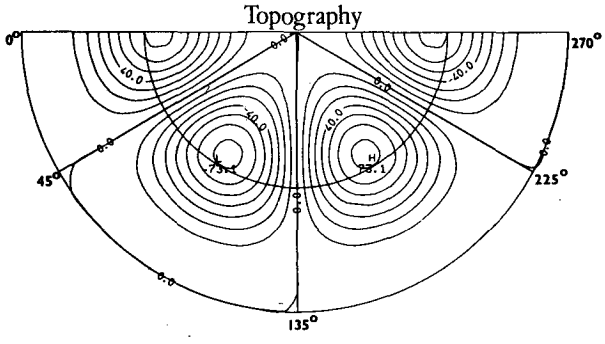

FIG. 2. Contours of the effective orography μh, $\mu = \sin\theta$. This is a conformal conical projection of ratio 2/3. The two half-circles in the figure correspond to the equator and the 45°N parallel. Topographic maxima and minima are indicated by H and L, respectively. The same projection is used in all subsequent flow-field maps.

The right-hand side of (1) models, at the same time as the forcing by ψ^*, the dissipation across a hypothetical Ekman layer. The characteristic relaxation time α^{-1} in midtroposphere, at the equivalent barotropic level, is usually taken to be of the order of 10 days (Charney and DeVore, 1979).

The energy of the flow E is the sum of the *kinetic* energy $K = -\int\int \psi\Delta\psi d\mu d\phi$ and of the *potential* energy $P = \int\int \lambda^{-2}\psi^2 d\mu d\phi$ associated with the free surface displacement. The constant $-\lambda^{-2}$ in the deformation term of (3) has the same sign as the eigenvalues of the Laplacian and therefore, its presence reduces the phase speed of free Rossby waves in the model [Pedlosky, 1979, Eqs. (3.18.6, 3.18.9)]. This reduction brings the interaction between planetary waves closer to nonlinear resonance. The effect discussed is purely dynamic, since the deformation term $\lambda^{-2}\psi$ disappears from the steady-state version of (3).

The dimensional radius of deformation L_R is taken equal to 1100 km throughout, except at one point in Section 5, where $L_R = \infty$. The value of 1100 km is a heuristic interpolation between an internal, baroclinic radius of deformation and the external barotropic one.

Substituting the truncated expansion of the variables (4, 5) in Eq. (3), we obtain a system of $N = 25$ ordinary differential equations for the N-vector $\Psi(t)$ with components $\psi_l^m(t)$. To write this system explicitly would be tedious and uninformative, so we give it in compact vector-matrix form:

$$\frac{d}{dt}\Psi = \rho\Psi^T\mathbf{B}\Psi + \mathbf{A}\Psi + \mathbf{C}, \tag{6}$$

where Ψ^T is the row-vector transpose of the column-vector Ψ, while $\mathbf{B}$ is a third-order tensor and $\mathbf{A}$ a usual, second-order tensor. The first term on the right-hand side contains the quadratic terms coming from the truncated Jacobian $J_T(\Psi, \Delta_T\Psi)$, the second term groups the linear terms from the Coriolis effect, orography and dissipation, and the last term represents the zonal forcing. Notice that the truncated Laplacian Δ_T acts on each component of Ψ exactly like Δ itself, i.e., as multiplication by $-l(l + 1)$.

System (6) is the object of this study. It is autonomous, i.e., the right-hand side

$$\mathbf{G}(\Psi; \rho, \alpha) = \rho\Psi^T\mathbf{B}\Psi + \mathbf{A}\Psi + \mathbf{C} \tag{7}$$

depends on time only through the dependent variables $\Psi = \Psi(t)$. The system is also forced, $\mathbf{C} \neq 0$, and dissipative, i.e., $\mathbf{X}^T\mathbf{A}\mathbf{X} < 0$ for arbitrary vectors $\mathbf{X} \neq 0$.

It can be shown that the solutions of (6) exist for all times $-\infty < t < +\infty$ and are unique for arbitrary initial conditions (Arnold, 1978, Sec. 7.7). Furthermore, as $t \to \infty$, the flow in the system's phase space

is volume reducing, and tends to certain attracting sets: fixed points, limit cycles, invariant tori, or strange attractors (Lorenz, 1963; Ruelle, 1984). We shall investigate the relationship between some detailed properties of the system's attractors and certain characteristics of large-scale midlatitude atmospheric flow discussed in Section 1.

3. Stationary solutions

a. Methodology

We study first the nature of the model's stationary solutions and follow their behavior as the parameters α and ρ change. This will help us examine later the nonstationary flow regimes.

For α large, tending to infinity, and ρ fixed, the stationary solution of (3) is clearly unique and tends to ψ^*. For ρ large, tending to infinity, and α fixed, there still exists a stationary solution tending to ψ^*, which is not necessarily unique. In the limit $\rho \to 0$, an equilibrium is reached which stays near ψ^* if α is at least of the same order as h. It may be shown (Legras and Ghil, 1983, hereafter LG1; also Appendix A) that these three asymptotic forms of the solution are stable with respect to time-dependent perturbations. The same results hold for the discrete system (6).

Between these limits lies the interesting domain of the parameter space. In the model of Charney and DeVore (1979; CDV hereafter), and other quasi-linear models with a very small number of degrees of freedom (three–six), the algebraic system corresponding to our

$$\mathbf{G}(\Psi; \mathbf{r}) = 0 \tag{8}$$

could be solved analytically to yield the stationary solutions $\Psi = \Psi(\mathbf{r})$, for all parameter values $\mathbf{r}$. In the present model, (8) represents 25 nonlinear algebraic equations, $\mathbf{r} = (\rho, \alpha)$, and one has to take recourse to numerical methods of solution.

The basic idea of the method used systematically here belongs to the class of continuation methods. Knowing a solution Ψ_0 for a given parameter value $\mathbf{r}_0$, $\mathbf{G}(\psi_0; \mathbf{r}_0) = 0$, one searches for solutions $\Psi(\mathbf{r})$ near the point $(\Psi_0, \mathbf{r}_0)$ by using

$$\frac{\partial \mathbf{G}}{\partial \Psi}(\Psi - \Psi_0) + \frac{\partial \mathbf{G}}{\partial \mathbf{r}}(\mathbf{r} - \mathbf{r}_0) = 0, \tag{9}$$

where $\partial \mathbf{G}/\partial \Psi$ and $\partial \mathbf{G}/\partial \mathbf{r}$ are matrices of partial derivatives evaluated at

$$(\Psi, \mathbf{r}) = (\Psi_0, \mathbf{r}_0).$$

The particular method employed is *pseudo-arclength continuation* (Keller, 1978). It solves (9) as an ordinary differential equation in the arclength s given by $ds^2 = \|d\Psi\|^2 + \|d\mathbf{r}\|^2$, using a predictor-corrector method. Here $\|\mathbf{X}\|$ stands for the length of the vector $\mathbf{X}$, in the appropriate dimension of Euclidean space, namely $N = 25$ for the phase space of Ψ and $p = 2$ for the parameter space of $\mathbf{r}$. The correction step uses a Newton-type technique for Eq. (8).

This continuation method allows one to explore completely a one-parameter solution branch of stationary solutions. It eliminates the difficulties encountered in other methods at regular turning points of a branch, where the rank of the matrix $\partial \mathbf{G}/\partial \Psi$ in (9) is less than maximal. A simple exposition of this method and technical details on its application to the present problem are given in Appendix B. Still, no method provides automatically the entire picture of all possible stationary solutions for the full $N \times p$-dimensional phase-parameter space. The picture may be filled in by carrying out a large number of explorations following different directions in parameter space. This approach, given some empirical ingenuity, provides redundant information and allows one to connect sheets of solutions which may appear as separate branches in certain one-parameter cross sections of the parameter space.

b. Dependence on parameters

In order to describe the distribution of stationary solutions as a function of the parameters, we have plotted in Fig. 3 the square root of their total energy $E = K + P$ as a function of ρ for different values of α. For $\alpha^{-1} = 1.1$ days (curve A in Fig. 3a) we are in the asymptotic domain of large α and the unique solution branch differs little from ψ^* for all ρ. In the sequel, α will always be given in day^{-1}, while ρ is nondimensional.

As α decreases, the relaxation no longer compensates for the destabilization of the mean flow by the orography, and waves are produced which interact with each other and feed back energy to the mean flow. As a result, the solution branch above is continuously distorted into a family of stationary solutions which has notably smaller energy than ψ^* and is characterized by a strong flux of energy extracted by the waves from the mean flow (curves B and C).

For $\alpha^{-1} \approx 5.25$ days, a fold develops in this solution branch near $\rho = 0.5$, analogous to the one observed in the CDV model. This fold leads to the existence of three stationary solutions for the same value of the parameters (curve D of Fig. 3a). Such a fold was also observed in Källén's (1984, Fig. 1) extension of the CDV model to the sphere.

As α decreases further, we see (curve E, Fig. 3b) an isolated closed branch, or isola, which detaches itself from the main branch for $\alpha^{-1} \geqslant 8.5$ days and is present for $0.18 \leqslant \rho \leqslant 0.20$, down to small values of α. Next, another fold appears for $\alpha^{-1} \approx 11$ days at $\rho \approx 0.20$ and develops for $\alpha^{-1} \geqslant 15$ days (curve G, Fig. 3c, and curve I, Fig. 3e) into a complicated structure.

In order to compare these results with those of CDV, we performed a similar analysis on a quasi-

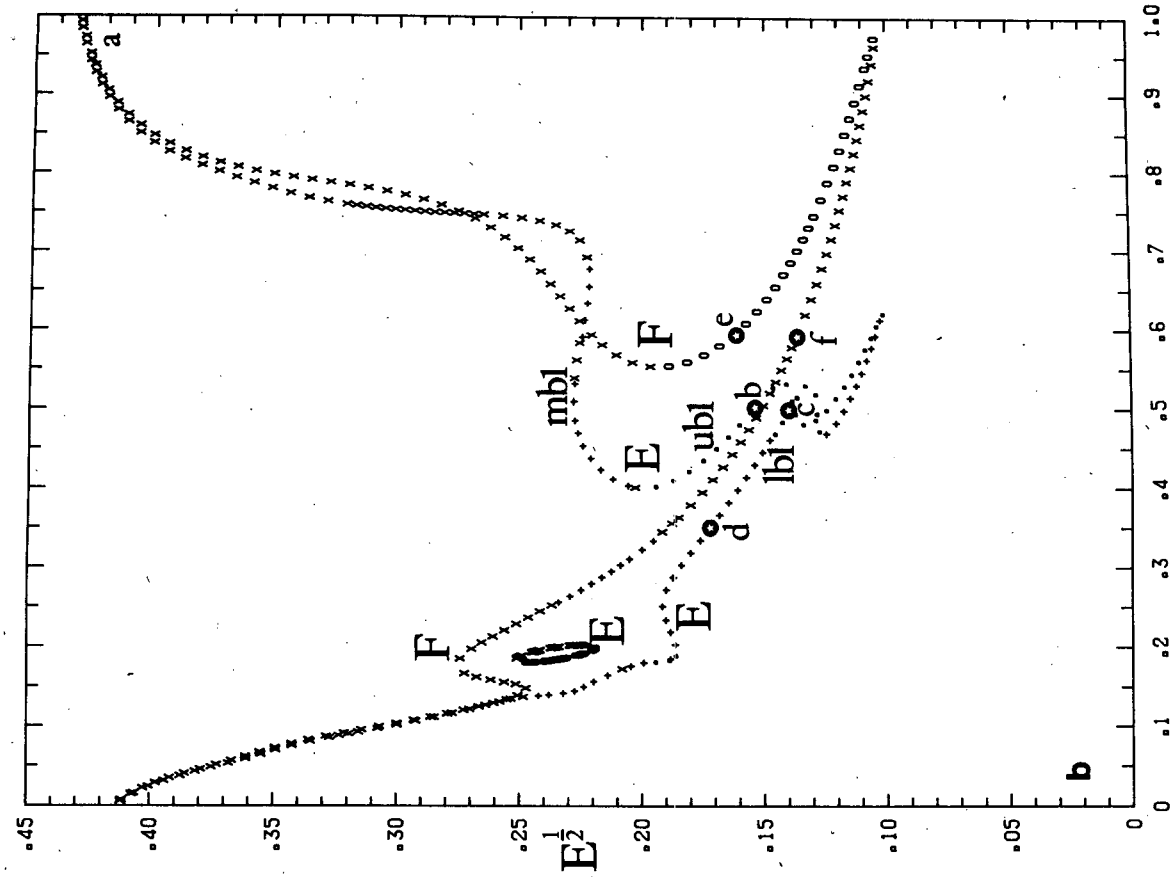

FIG. 3b

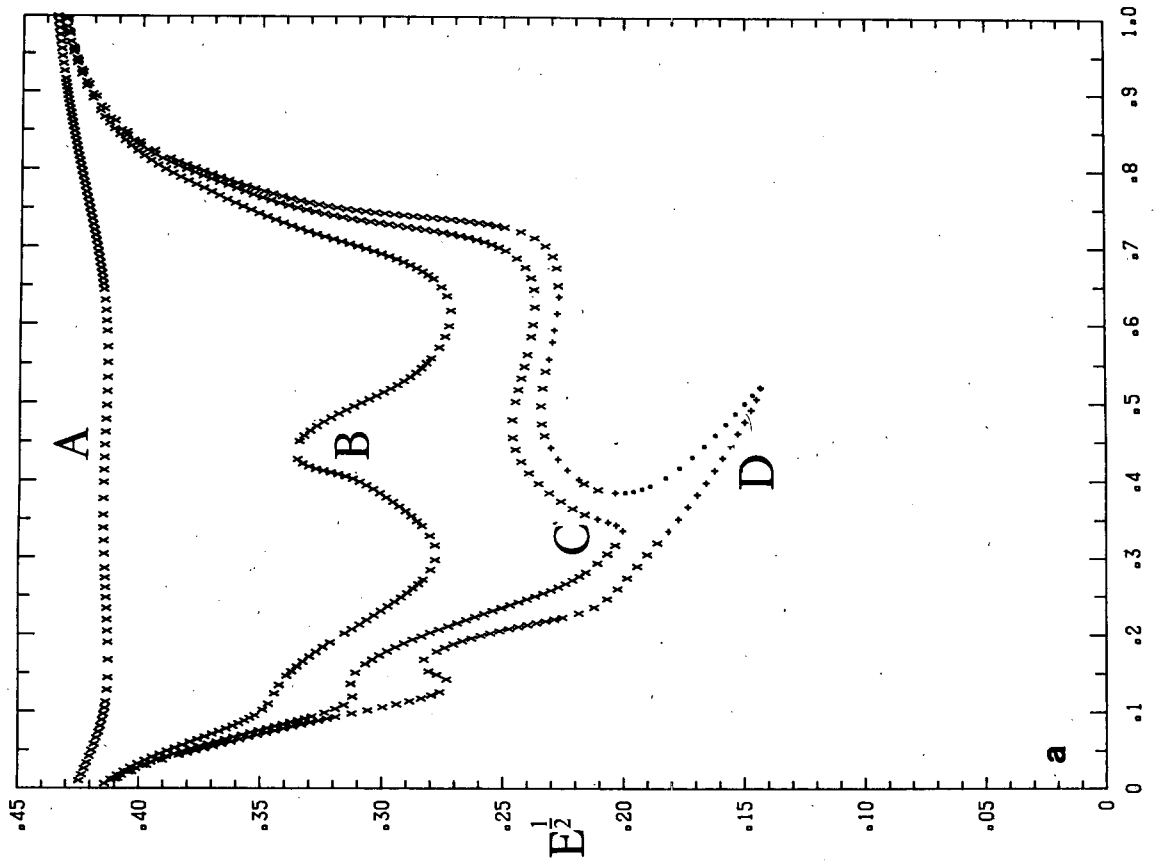

FIG. 3a

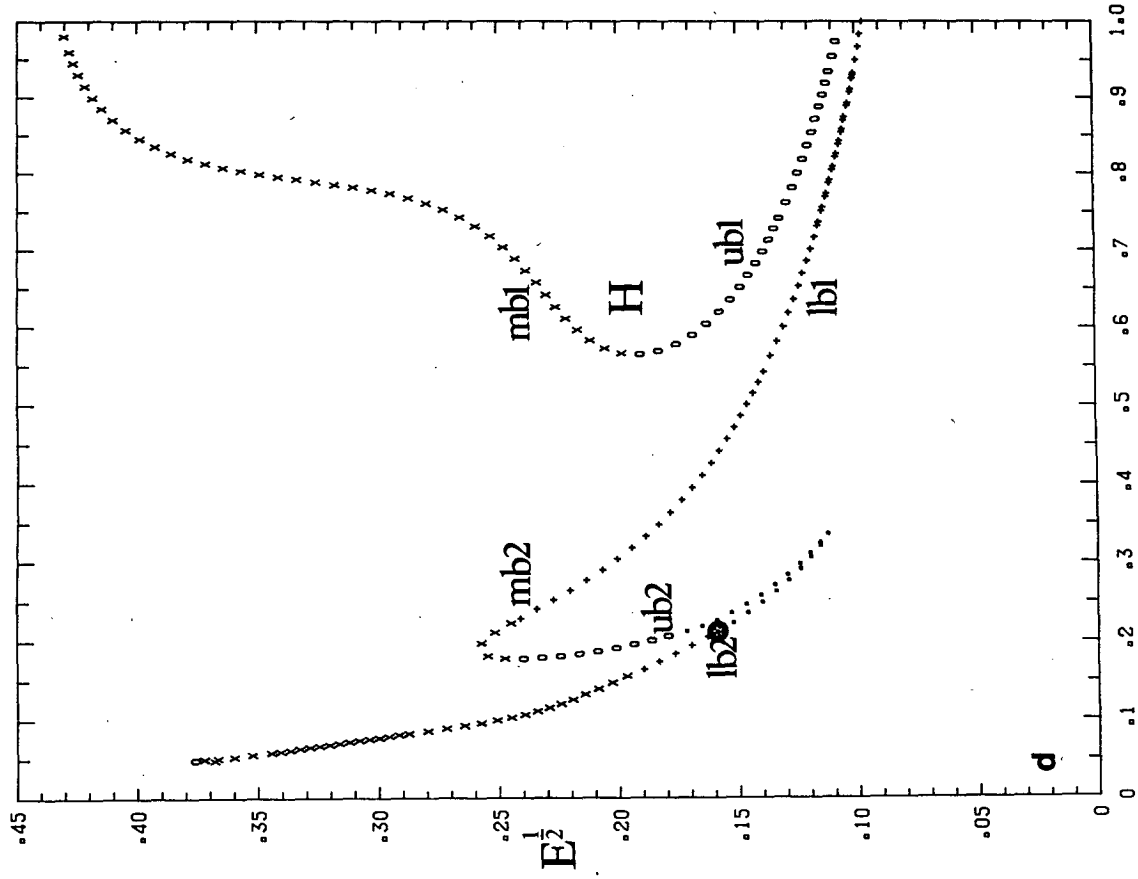

FIG. 3d

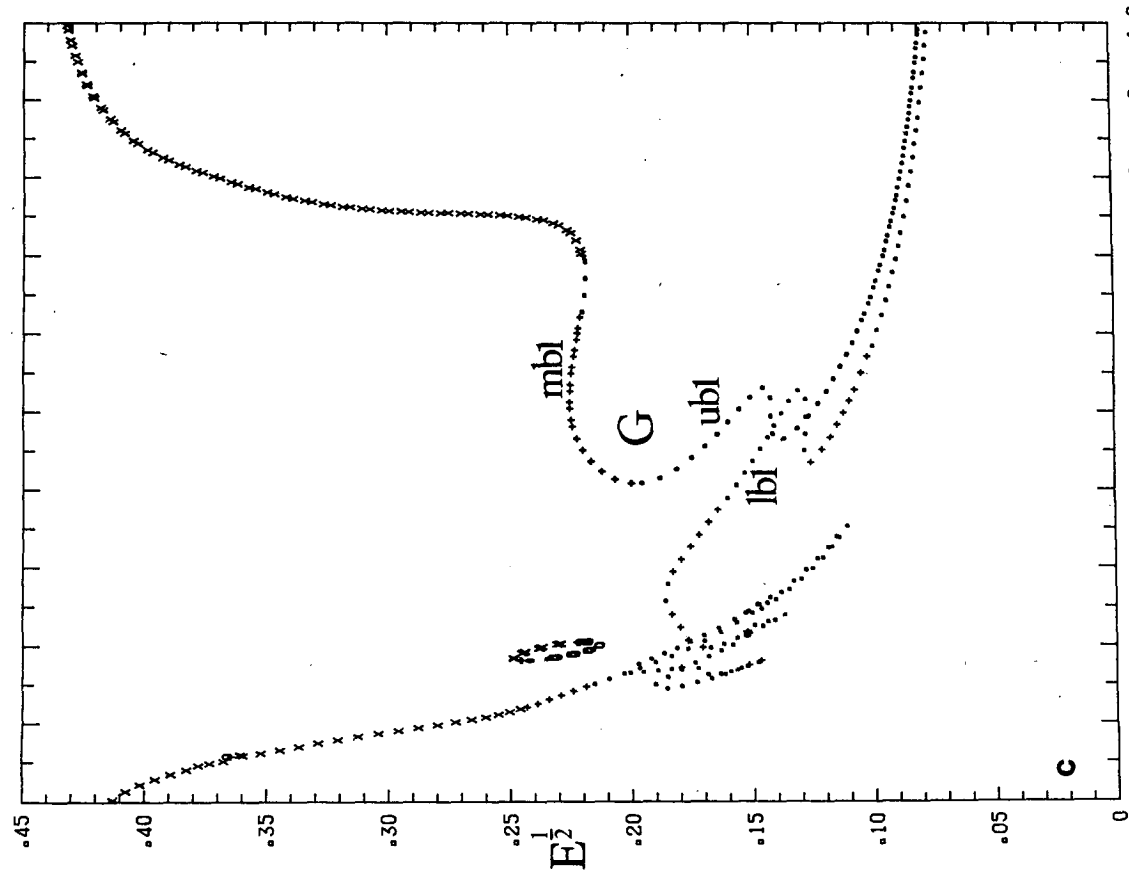

FIG. 3c

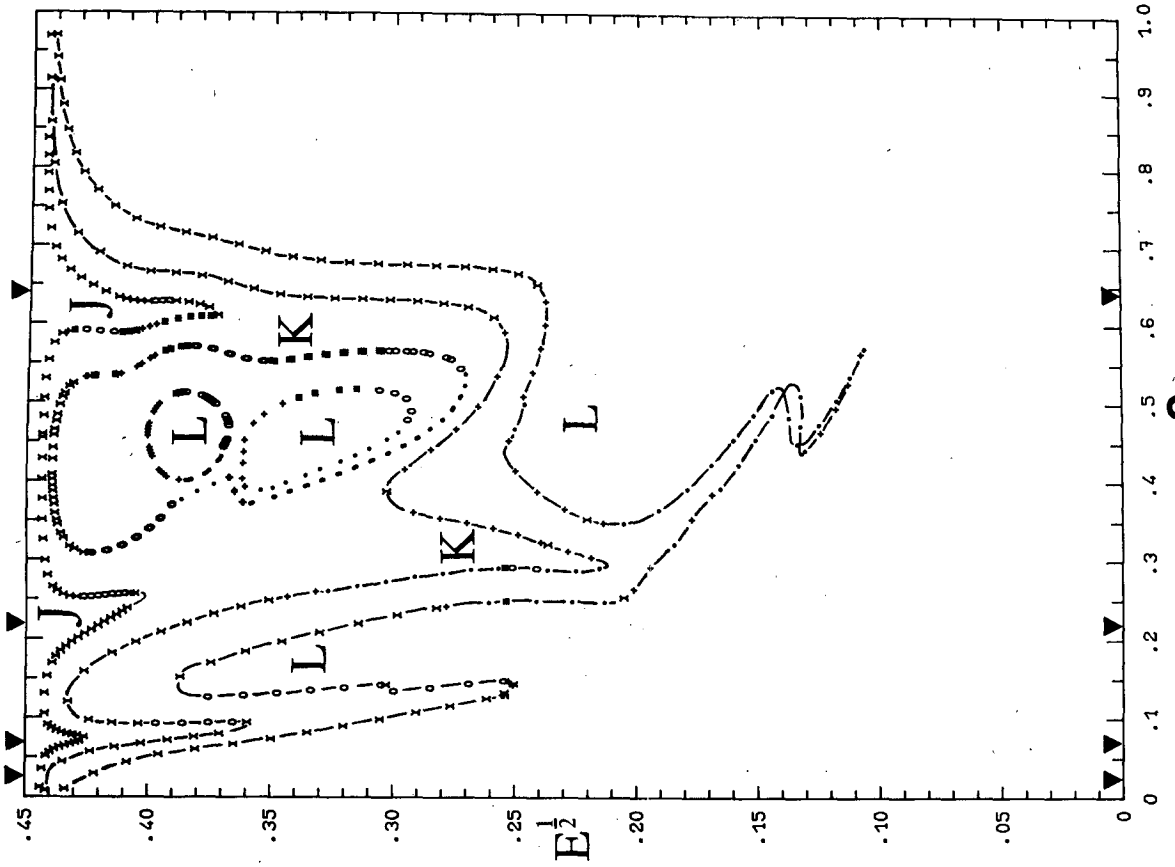

FIG. 4

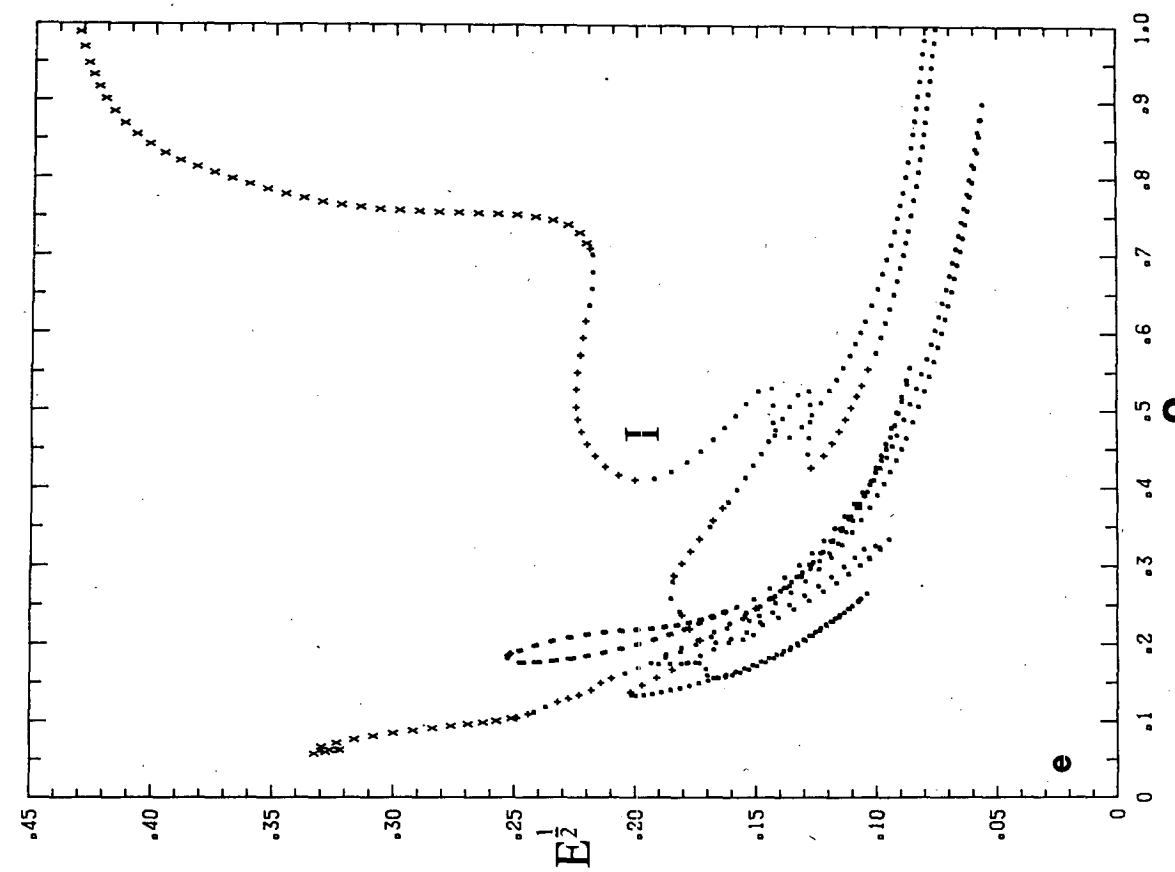

FIG. 3e

FIG. 3. Total energy E of stationary solutions as a function of the forcing parameter ρ for several fixed values of the dissipation parameter α, and for $h_0 = 0.1$ [see Eqs. (2b, 5a)]. The stability of the solutions is denoted by the following symbols: cross, stable solution; open circle, plus, asterisk, closed circle, unstable solutions for which the eigenvalues of the linearization $\mathcal{L}_s$ with positive real part are respectively: open circle, one real eigenvalue; plus, two complex conjugate eigenvalues; asterisk, two real eigenvalues; closed circle, at least three eigenvalues. Values of α^{-1} in days: (a) A, $\alpha^{-1} = 1.1$, B, $\alpha^{-1} = 3.3$; C, $\alpha^{-1} = 5.0$; D, $\alpha^{-1} = 6.7$. (b) E, $\alpha^{-1} = 10.0$; F, $\alpha^{-1} = 10.0$, quasi-linear model (c) G, $\alpha^{-1} = 20.0$ (d) H, $\alpha^{-1} = 20.0$, quasi-linear model (e) I, $\alpha^{-1} = 33.0$. The labeling of various branches is explained in the text. Stars indicate stationary solutions for which the flow patterns appear in Fig. 5 (curves E and F) and Fig. 7d (curve H).

FIG. 4. Total energy E of stationary solutions as a function of the forcing parameter ρ for $\alpha^{-1} = 20$ days and several fixed values of the orographic amplitude h_0. Stability symbols are as in Fig. 3. Values of h_0 are: J, $h_0 = 0.01$; K, $h_0 = 0.02$; L, $h_0 = 0.05$. The solid pointers on the abscissa indicate linearly resonant values of ρ for vanishing h_0.

linear version of our model, in which all wave–wave interactions were suppressed. In this new system, the nonzonal components of a stationary solution satisfy a linear system with coefficients depending on the zonal state. This system shows nonlinear resonances for some values of the zonal flow due to the existence of small denominators.

For arbitrary parameter values, the quasi-linear stationary solutions obtained have all components with zonal wavenumber $m \geqslant 4$ equal to zero. Time-dependent integrations of the quasi-linear model show that perturbations with $m \geqslant 4$ in a nonstationary solution decay to zero in time. Since the only forced modes have $m = 0$ and $m = 2$, and since no interactions between $m = 2$ and $m \geqslant 4$ are present, it follows that in the quasi-linear model the mean flow is *barotropically stable.*

Figures 3b (curve F) and 3d (curve H) show the cross sections $E = E(\rho)$ of the quasi-linear model for $\alpha^{-1} = 10$ and 20 days. The large resonance observed in both figures for $\rho \geqslant 0.5$ is the image of the CDV orographic instability mechanism in the present model.

The difference between the upper branch of the resonance (marked by *ub1* in Figs. 3b and 3e) and the main branch (marked *mb1*) consists essentially of a decrease of the zonal component of the flow. Between the upper branch (*ub1*) and the lower branch (*lb1*), on the other hand, there is little change in the zonal component, but a global westward phase shift of the energy containing components $(l, m) = (3, 2)$ and $(5, 2)$ without modification of their amplitude, as in CDV and in Källén (1984, Fig. 3). Similar results were also obtained by Davey (1981) with a quasi-linear model in an annular geometry.

Notice that the exact value of the phase shift depends on α in this model, as well as in the three preceding ones. It is also clear that, in the fully nonlinear model, wave–wave interactions limit further the ρ-extent of the quasi-linearly resonant fold (compare curve E with curve F in Fig. 3b).

The second resonance, noticed already for the fully nonlinear model, is also visible, especially in Fig. 3d. It can be shown (Appendix C) that this second resonance, appearing at more realistic values of ρ, $\rho \leqslant 0.30$, is due to the addition of more degrees of freedom in the meridional direction: the number of folds in the resonance pattern increases with the number of meridional modes, but most of them accumulate near $\rho = 0$.

This resonance is different in character from the first one. In the quasi-linear model, a uniform westward phase shift between its upper branch (*ub2* on curve H) and its lower branch (*lb2*) affects the modes (5, 2), (7, 2) and (9, 2), but the largest-scale mode (3, 2) remains unchanged. This indicates that the resonance develops on a basic flow which, far from being zonal, possesses a strong wave component.

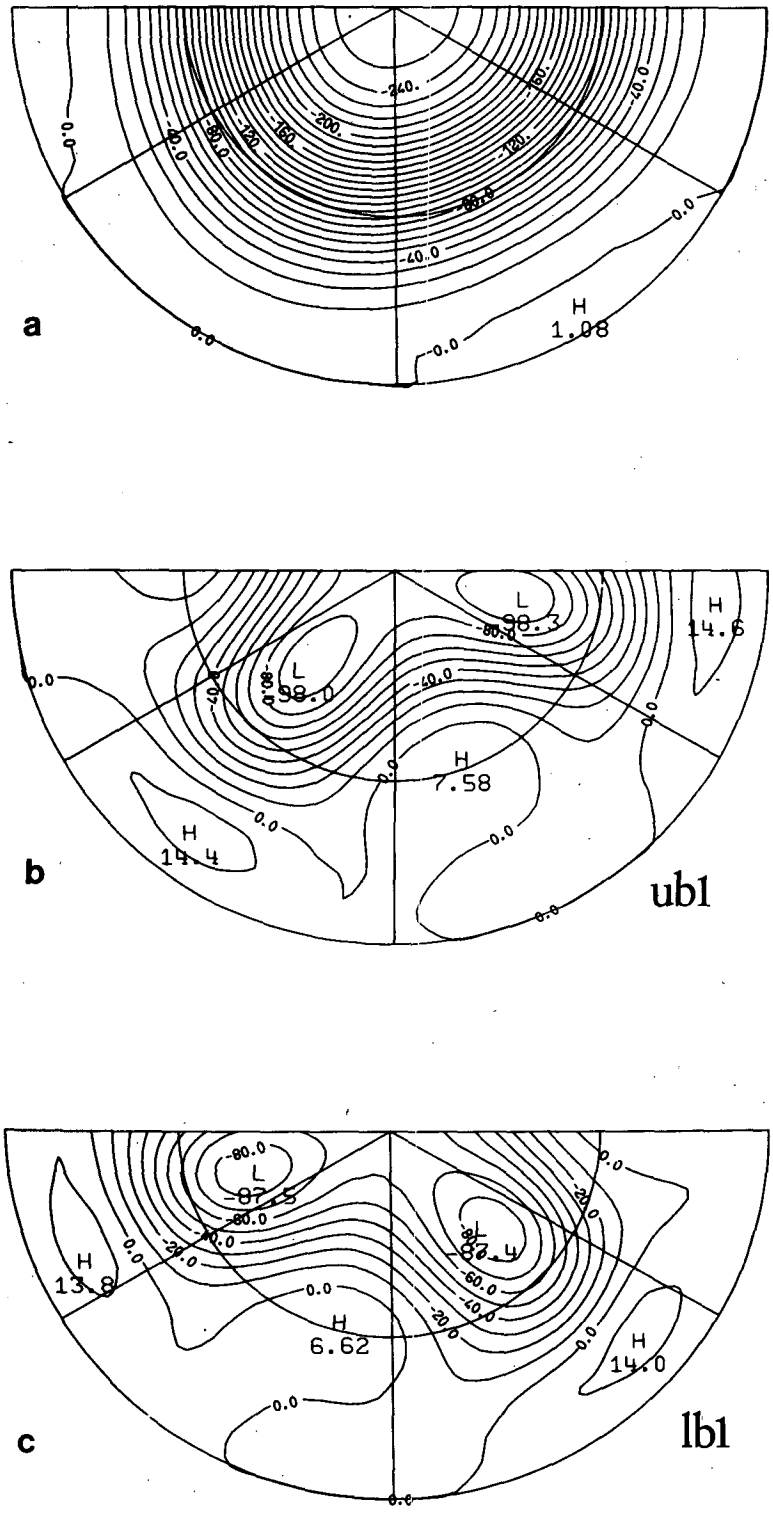

FIG. 5. Contours of the streamfunction Ψ for stationary solutions; $\alpha = 0.1$. Projection as in Fig. 2. Contour intervals are 10 nondimensional units [see Eqs. (2d, e)]; to obtain ψ in geopotential meters, the plotted values have to be multiplied by 61.9ρ. (a) $\rho = 1.25$; (b) $\rho = 0.5$, upper branch of the first resonance; (c) $\rho = 0.5$, lower branch of the first resonance; (d) $\rho = 0.35$, main branch between the first and second resonance; (e) $\rho = 0.6$, upper branch of the first resonance, quasi-linear model; (f) $\rho = 0.6$, lower branch of the first resonance, quasi-linear model.

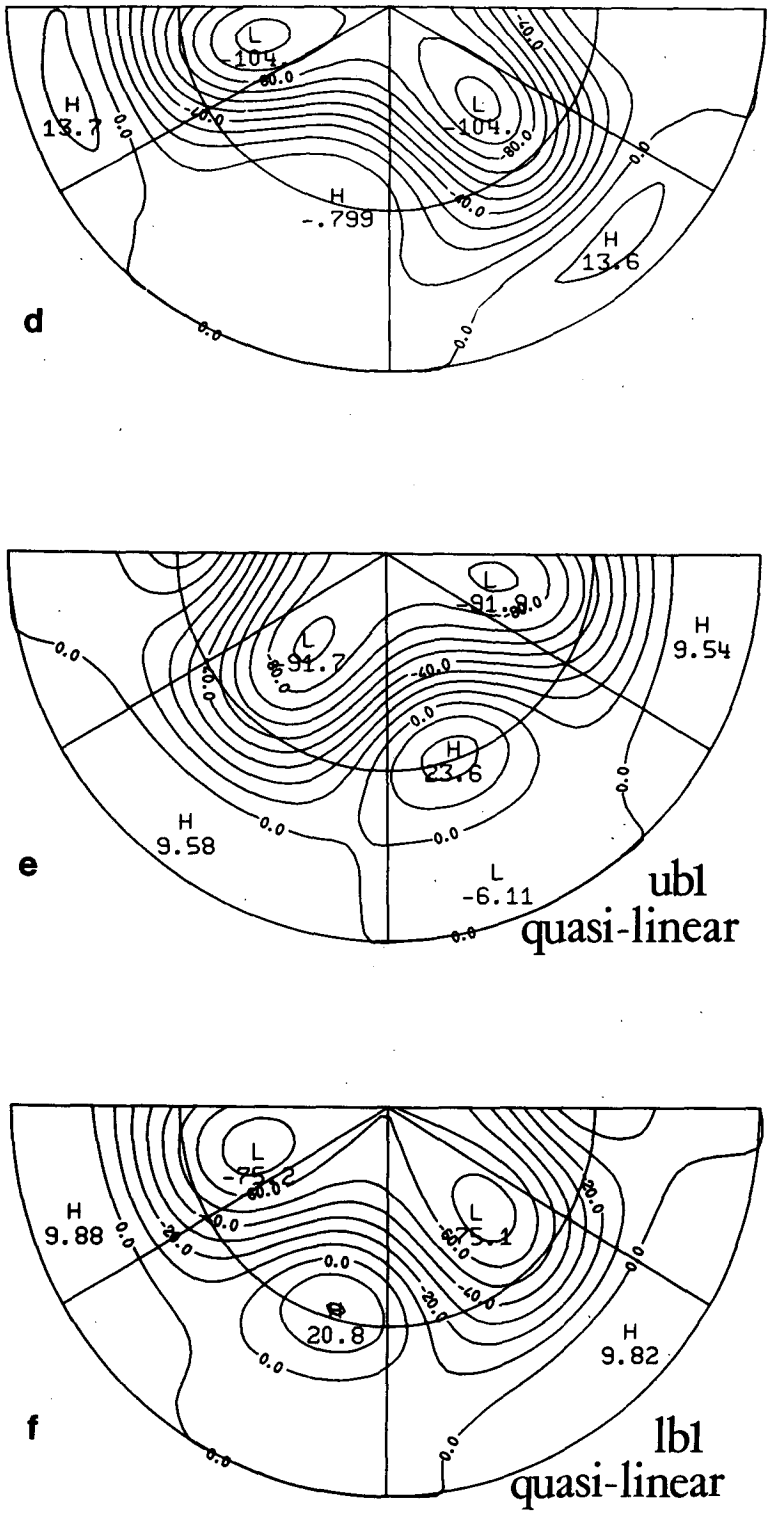

FIG. 5 (*Continued*)

In the fully nonlinear model (Fig. 3c), the first resonance keeps the appearance of a unique distorted fold. The second one exhibits a more complicated structure where, as α decreases, new folds develop on the already existing ones in a seemingly endless cascade. The ρ-extent of the folds grows considerably

as α goes to zero (Fig. 3e). Comparing Fig. 3c with Fig. 3d, we see that the isolated branch, associated with the second resonance in the nonlinear model, is presumably due to the reconnection of branches *mb2* and *ub2* of the quasi-linear model.

To study further the genesis of both resonances in the nonlinear model, we show in Fig. 4 the $E = E(\rho)$ curves for $\alpha^{-1} = 20$ days and for several values of h_0, taken here as a third parameter of the problem. For very small values of h_0 and α, we solve in Appendix C the stationary problem assuming that ψ is a small perturbation of ψ^*. Three linear resonances are found at the values $\rho_0^R = 0.65$, $\rho_1^R = 0.21$ and $\rho_2^R = 0.07$ of the forcing parameter. They are directly associated with the three resonances observed for $h_0 = 0.01$ (curve J, Fig. 4).

As h_0 increases, the resonances develop towards lower energy and nonzonal flows. For $h_0 = 0.025$ (curve K, Fig. 4) the ρ_0^R- and ρ_1^R-resonances become connected, leaving a big isola of relatively zonal flow. For $h_0 = 0.050$ (curve L, Fig. 4), we have recovered a large part of the picture shown in Fig. 3c, where $h_0 = 0.1$.

The ρ_0^R-resonance does not lead to a fold; connected with the ρ_1^R-resonance, it produces the knee of the branch *mb1*. The ρ_1^R- and ρ_2^R-resonances lead to the first and second resonances in the nonlinear model, respectively.

For $h_0 = 0.05$, the first fold has smaller ρ-extent than for $h_0 = 0.1$, and the second resonance is not yet folded. The big isola for $h_0 = 0.025$ has split into a twin system for $h_0 = 0.050$. When h_0 increases further, these two isolas decrease in size and eventually collapse. The isola obtained for $h_0 = 0.1$ (Fig. 3c) is the trace of a larger branch generated between $h_0 = 0.05$ and $h_0 = 0.1$. It in turn disappears for $h_0 = 0.2$ (not shown).

As the topographic height parameter h_0 increases, it induces more coupling between the modes of the model, resulting in more nonlinearity. The sequence of curves $E = E(\rho)$ as a function of increasing h_0 is quite similar to the sequence observed as the dissipation parameter α decreases. The connection with linear resonances at small h_0 demonstrates in the present case the continuity between linear and nonlinear models. It shows also that the complete behavior of the nonlinear model can hardly be inferred from a linear analysis (see also Itoh, 1985).

c. *Flow patterns*

The spatial resolution provided by the model allows comparatively complex flow patterns to appear. The description of the ensemble of patterns appearing as stationary solutions is facilitated by the fact that these depend relatively little on α along a given sheet of solutions. This result was expected for large and for small values of ρ (cf. Appendix A), but holds also true for intermediate values.

Figure 5 shows the most important flow patterns appearing for large values of ρ, near the CDV resonance: panels 5a–d follow the changes along curve E in Fig. 3b, while 5e–f represent points on curve F. The flow in Fig. 5a, for $\rho = 1.25$, differs only very slightly from ψ^*. The nonzonal part of the flow is dominated by the directly forced wavenumber $m = 2$, which is in phase with the orography. The dependence on α ($\alpha = 0.1$ day^{-1} for all panels in the figure) is negligible.

As ρ decreases, the deviation of the solution from ψ^* increases rapidly between $\rho \approx 1.0$ and $\rho \approx 0.7$. The nonzonal component is slightly shifted westward and becomes stronger, leading to the appearance of a closed pressure center above "mountains," i.e., above the positive orographic heights (LG1, Fig. 5b; compare also our Fig. 5e).

Changes are small between $\rho \approx 0.7$ and $\rho \approx 0.4$, where the turning of the main branch *mb1* into the CDV resonance occurs. The dependence on α consists in an eastward shift of the high-pressure center (marked H in the figures) relative to the mountains as α decreases, causing less energy to be drawn from the mean flow [see also Eq. (A3)]. Among nonzonal modes, $m = 2$ is still most prominent.

For both branches of the CDV resonance, $m = 2$ is also dominant. The upper branch *ub1* of this resonance (Fig. 5b) has a zonal flow only half as strong as that of the main branch *mb1* above it, while the nonzonal part of the flow is intensified, keeping the same phase. The lower branch *lb1* (Fig. 5c) shows a pattern similar to that of the upper branch, but shifted westward by 60°, which produces a strong northerly flow into the western half of the "continents." These flow characteristics allow one to associate the solutions on the main branch *mb1* for $\rho \geq 0.5$ and on the lower branch *lb1* of this first resonance with the solutions called "zonal" and "blocked" respectively by CDV.

The main features of the lower branch are unchanged for smaller values of ρ, down to $\rho \approx 0.20$, where the second turning point occurs. Figure 5d shows this flow pattern in a region of parameter space where it is the unique stationary solution ($\rho = 0.35$ and $\alpha^{-1} = 10$ days). When α decreases, the pattern is shifted further westward, until the low-pressure center (marked L in the figure) is at the same longitude as the maximum topographic height.

The stationary solutions of the quasi-linear model (curve F in Fig. 3b) are shown in Fig. 5e for the upper branch and in Fig. 5f for the lower branch of the CDV resonance. They exhibit the same features as the corresponding solutions of the full model, due to the dominance of wavenumber $m = 2$ in the solutions of either model. The fact that the corresponding features here are somewhat more pronounced than in the full model is due to the total absence of high wave number energy in the quasi-linear model.

We saw already in Section 3b that a second resonance occurs in our model at lower, more realistic values of the forcing parameter ρ. This second resonance has a more complicated structure than the CDV resonance, involving mostly the modes of degree $l \geqslant 5$. The detailed structure of the enlarged $E^{1/2}$ versus ρ curve for $\alpha^{-1} = 20$ days (curve G in Fig. 3c) is shown for the neighborhood of $\rho = 0.20$ in Fig. 6.

In this region of parameter space, the solutions' flow patterns can be classified into four families—Blocking, Zonal 1, Zonal 2 and Double Block—which correspond to the various branches as denoted in Fig. 6. Representative examples of the solution families identified in Fig. 6 are shown in Fig. 7. Inside each family there exist amplitude and phase variations, but the general pattern of the solution remains un-

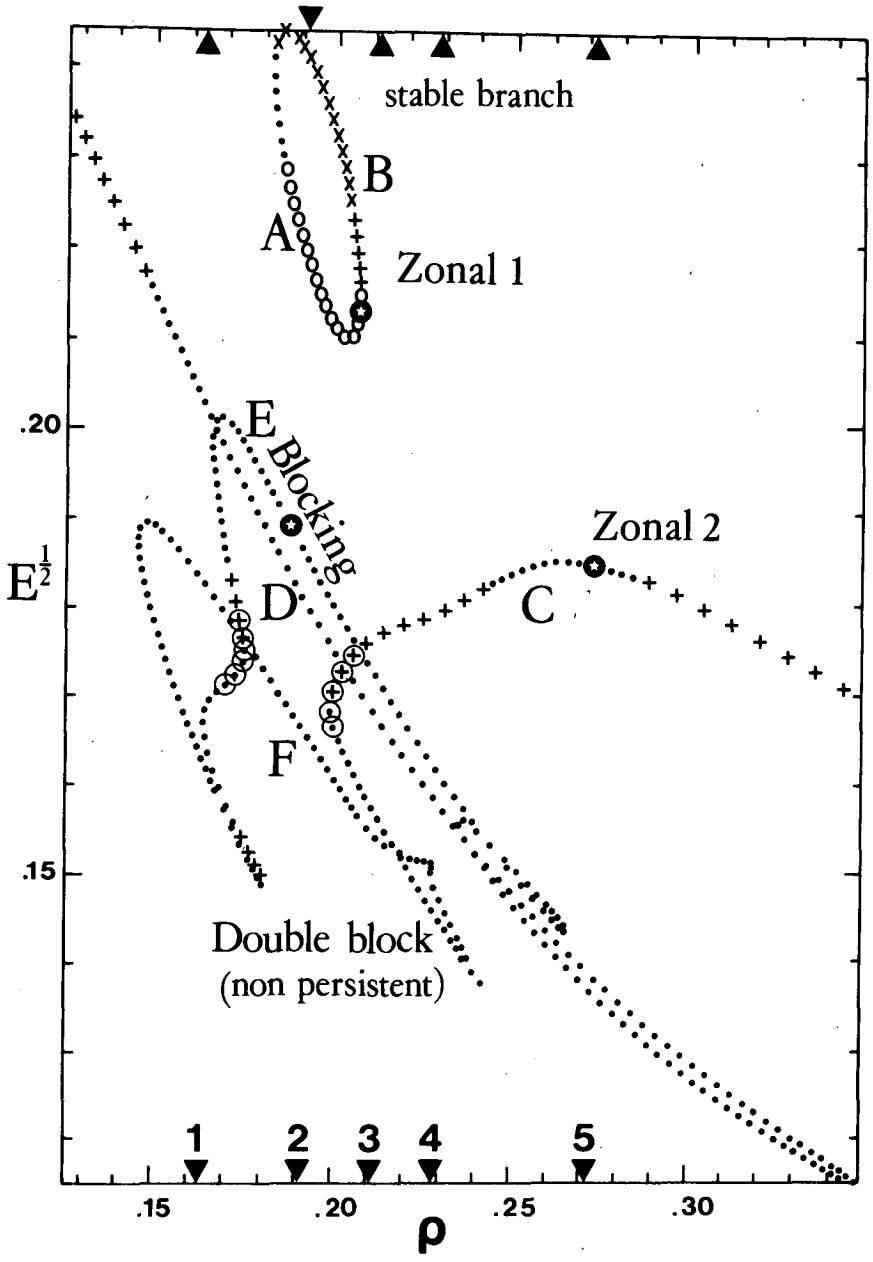

FIG. 6. Blow up of a portion of Fig. 3c. Stationary solution branches associated with the second resonance for $\alpha^{-1} = 20$ days. Stability symbols as in Fig. 3. Branch segments circled show rapid transitions between Blocking, Double Block and Zonal 2 type flow patterns. Numbered pointers on the abscissa indicate values of ρ for which time-dependent model solutions are investigated in detail. The flow patterns of stationary solutions marked by stars appear in Figs. 7a–c.

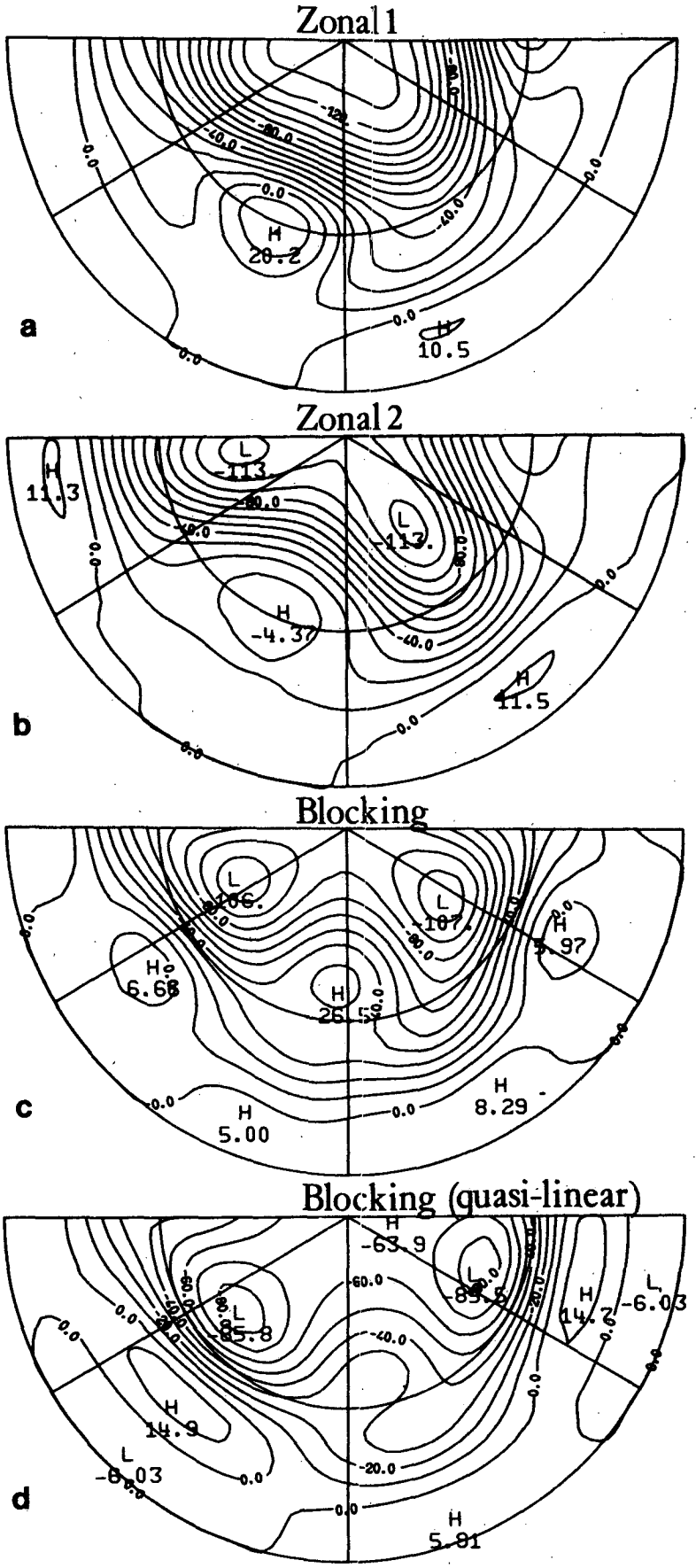

FIG. 7. Flow patterns of the stationary solutions indicated by stars in Fig. 6: (a) Zonal 1; (b) Zonal 2; (c) Blocking; and in Fig. 3d: (d) Blocking in quasi-linear model (curve H).

changed. Transitions along branches between Blocking, the Double Block and Zonal 2 occur quite sharply in the circled segments of Fig. 6.

The Zonal 1 flow (Fig. 7a), associated with the isolated branch, has a high energy level: the maximum intensity of its zonally-averaged jet is 50 m s^{-1}. The Zonal 2 flow (Fig. 7b) is less intense, with a 35 m s^{-1} jet in zonal average. Both of these zonal flows exhibit, in fact, a ridge on the west side of the orography and a trough on the east side, similar to the averaged winter circulation of the Northern Hemisphere. They may thus be associated with the regular weather regime, and we shall do so in the sequel.

The west coast ridge is strongly intensified in the blocking solution (Fig. 7c), which shows a well developed high center on the west side of the orography, splitting the zonal flow into two jets. The averaged zonal wind is reduced to 18 m s^{-1} and the geopotential height difference between the trough and the ridge is about 1000 m. The exaggerated amplitude of this flow feature would presumably be reduced by thermal damping and by interactions with higher wavenumbers to the correct order of magnitude of 500 m.

We show also in Fig. 7d one solution of the quasi-linear model (curve H, Fig. 3d), located on the lower branch of the second resonance for the same value of the parameters as in Fig. 7c. Both patterns are quite similar, although the quasi-linear solution is shifted eastward and exhibits a weaker zonal wind.

Zonally-averaged zonal wind profiles as a function of latitude were calculated for all stationary solutions discussed in this section (not shown). The flow patterns apparent for $\rho \approx 0.2$ all have easterly winds in the tropics. The maximum easterly speed occurs at the equator and lies between 2 m s^{-1} and 8 m s^{-1}. This maximum speed is higher for the zonal than for the blocked stationary solutions, in qualitative agreement with the observations of Namias (1950, Fig. 5), for instance.

In the following section, we shall discuss the stability of the stationary solutions, and the role they have in organizing the model's phase-space flow. The double-block type of solutions (Fig. 5e in Legras and Ghil, 1984, LG2 hereafter) seems to play no role in the model's dynamics and hence is not shown here. The blocking solution and both zonal branches, on the other hand, will turn out to be important for time-dependent model behavior.

4. Stability and dynamics

a. *Stability of stationary solutions*

Linear stability of a stationary solution Ψ_s is determined by the spectrum of the linear operator $\mathcal{L}_s$ associated with the perturbation problem of time-dependent evolution in an infinitesimal neighborhood of Ψ_s. For any one of the stationary solutions above, $\mathcal{L}_s = \mathcal{L}(\Psi_s)$ is given by

$$\mathcal{L}_s\chi = (\Delta_T - \lambda^{-2})^{-1}\{\rho J_T(\Psi_s, \Delta_T\chi) + J_T[\chi, \rho\Delta_T\Psi_s + \mu(1 + h)] + \alpha\Delta_T\chi\}. \quad (10a)$$

The operator $\mathcal{L}_s$ is easily obtained as an $N \times N$ matrix from Eq. (6),

$$\mathcal{L}_s\chi = \rho(\Psi_s^T\mathbf{B}\chi + \chi^T\mathbf{B}\Psi_s) + \mathbf{A}\chi. \quad (10b)$$

Eigenvalues are then computed by a standard algorithm (see Appendix B). If all eigenvalues are in the left half of the complex plane, the solution Ψ_s is linearly stable. Otherwise it is linearly unstable.

Let Ψ_s be a stationary solution for which $\mathcal{L}_s$ has no eigenvalues with zero real part. Then the quadratic character of the nonlinearity in Eq. (6) insures that there exists in phase space a finite, small neighborhood $U = (\|\Psi - \Psi_s\| < \epsilon)$ of Ψ_s such that the following dichotomy holds: if Ψ_s is stable, then solutions $\Psi(t)$ of (6) with initial data in U, $\|\Psi(0) - \Psi_s\| < \epsilon$, stay in U and tend to Ψ_s as $t \to \infty$; if Ψ_s is unstable, then almost all solutions of (6) starting in U will leave it in finite time, so that there exist times $0 < t_1 \leq t \leq t_2$ for which $\|\Psi(t) - \Psi_s\| \geq \epsilon$. The excluded set of initial data in the latter case refers to the *stable manifold* of Ψ_s, which has, by the definition of Ψ_s as an unstable fixed point, dimension $s < N$ and hence volume zero; s being just the number of eigenvalues with negative real part. Details and proofs of these and related statements on the qualitative theory of ordinary differential equations, dynamical systems and bifurcation theory can be found in Arnold (1978, 1983) and Guckenheimer and Holmes (1983).

We shall see in Section 5 that trajectories of (6) do leave the neighborhood of a linearly unstable stationary solution. More interestingly, they can return after some time, $t > t_2$, to this neighborhood by following closely the stable manifold of the solution, and dwell there for long times. The persistence properties of such neighborhoods in phase space, and of the associated planetary flow regimes in physical space, will be explored numerically in Section 5.

As a first analytical step in this exploration, we return now to the linear stability properties of stationary solutions. These are shown in Figs. 3a–e and in Fig. 4: stable solutions are marked by a cross; unstable solutions are labeled to indicate the number u of eigenvalues with positive real parts (see captions).

This number is important for the nonlinear dynamics. The eigenvectors associated with the unstable eigenvalues span the solution's unstable tangent space, and $s + u = N$ for almost all points in phase-parameter space. The nonlinear extension of this tangent space is the *unstable manifold,* which has the same dimension u in a finite neighborhood of the solution. If $u \ll s$, then one may hope that the given unstable solution plays a significant role in the global, nonlinear dynamics.

The case in which $\Psi_s = \Psi_s(\mathbf{r})$ is such that some eigenvalues of $\mathcal{L}_s$ have zero real part, and hence s

$+ u < N$, corresponds to lower-dimensional manifolds, i.e., to points or curves in our two-dimensional parameter space, with $\mathbf{r} = (\rho, \alpha)$. The set of $\mathbf{r}$ for which $s(\mathbf{r}) + u(\mathbf{r}) < N$ has in general zero volume, or measure, in parameter space and is known as the *bifurcation set.*

Turning points on solution branches (Figs. 3 and 4), also called saddle-node bifurcations, are associated with a real eigenvalue passing through zero. Likewise, stationary solutions lose their stability to periodic solutions at points of Hopf bifurcation, where a pair of complex conjugate eigenvalues crosses the imaginary axis from the left into the right half-plane. The presence of three or more unstable eigenvalues indicates the possibility of aperiodic solutions (Lorenz, 1963; Ruelle, 1984).

As a rule, we found that the most stable solution of (6) at a given value of the parameters is the one with the highest energy. Solutions associated with resonances exhibit a relatively large number of unstable eigenvalues. This number increases along the resonant branches and as α decreases. The dimension u of the unstable manifold may exceed 10 on certain branches for $\alpha < 0.05$ day^{-1}.

Figure 8 shows the linear stability of the most stable stationary solution in the (α, ρ)-plane of parameters with $h_0 = 0.1$. Due to the remark above, this figure can also be seen as a plan view from the top of the $E = E(\rho, \alpha)$ surface whose cross sections appear in Figs. 3 and 6.

For $\alpha > 0.205$, a zonal solution, close to the forcing flow Ψ^*, is unique and stable. Solutions at very small and very large ρ are also stable for all α, in agreement with the asymptotic analysis of Appendix A.

As α decreases, instabilities associated with Hopf bifurcation develop for $0.1 < \rho < 0.75$. Each one of these instabilities gives rise to one of the hatched lobes in Fig. 8. These lobes grow in the (α, ρ)-plane in the direction of decreasing α, and eventually merge into one large hatched area, where no stationary solution is stable. The fact that stability decreases with decreasing dissipation is in accordance with our general fluid-dynamical intuition, and should hold for the continuous Eq. (1), as well as for the discrete, truncated model (6).

Within the hatched instability area, the turning line of the main branch mb1 into the upper branch ub1, and the two boundaries of the isolated, Zonal 1 branch are shown as solid lines, for $\rho \approx 0.4$ and near $\rho \approx 0.2$, respectively. The folding of the first resonance (solid) merges at point S with a Hopf bifurcation line (dashed in the figure). According to our numerical evidence, S is a triple bifurcation point, or critical point. The chaotic behavior in the neighborhood of this point will be discussed further in Section 4b.

The isolated branch with Zonal 1 flow patterns is always more stable than the other solutions which coexist with it at the same parameter values and at lower energies. We shall not discuss here the complicated bifurcation patterns to which the second resonance, lying under the isola, gives rise. Heuristically, the multiple folds of this nonlinear resonance seem to be related to the accumulation of linear resonances discussed in Appendix C.

Finally, we notice that multiple stable equilibria

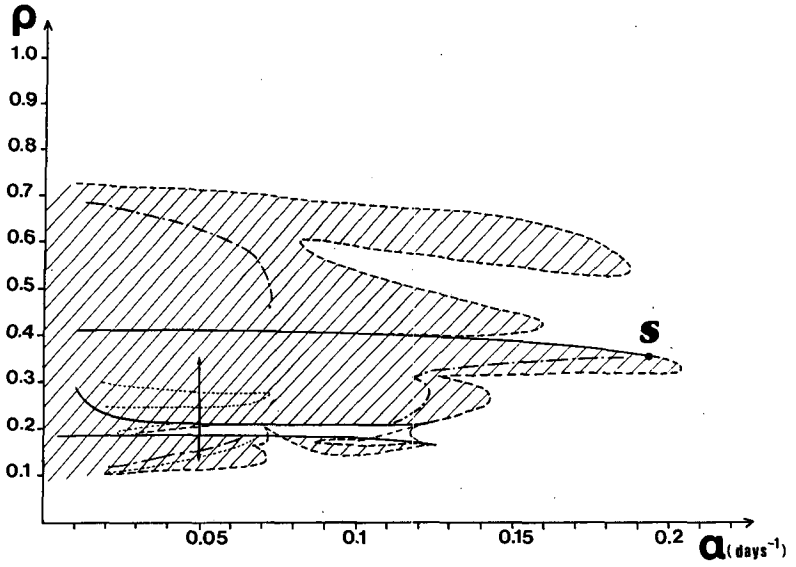

FIG. 8. Stability domain of the most stable solution as a function of ρ and α. Solid lines: regular turning line of the sheet of stationary solutions. Dashed lines: Hopf bifurcation of a stable stationary solution. Dotted lines: second Hopf bifurcation. Dash-dotted lines: the onset limit of chaotic regimes. The instability domain where no stable stationary solution exists is hatched. See text for discussion of point S.

occur in this model only in a very small parameter range, near $\rho = 0.18$ and $\alpha = 0.07$ (see Fig. 8). This situation has to be contrasted with the fact that multistable solutions are characteristic of wide parameter ranges in simpler, more highly truncated or quasi-linear models (cf. CDV; Källén, 1984; and Figs. 3b, d here).

For multiple flow regimes to exist in the present model over a wider range of parameter values, they must therefore be related to the existence of higher-dimensional attractors. The discussion of stable and unstable manifolds following Eq. (10) and the study of bifurcation patterns in Fig. 8 lead us to expect that parts of such complicated attractors might lie close to unstable fixed points or even contain such points (as in the case of the Lorenz attractor; cf. Lorenz, 1963). We shall also see in Section 5 that very persistent flow pattern evolutions in physical space can be explained by the proximity of a turning point on a stationary solution branch in phase space.

b. *Periodic and aperiodic solutions*

In the previous subsection, we have seen how stationary solutions lose their stability by bifurcations which give rise in general to periodic and aperiodic solutions. To study such solutions and the flow patterns associated with them in detail, a large number of numerical integrations of the evolution equation (6) were carried out. Numerical solutions were computed for hundreds of values of the parameters and various initial data, each solution being computed for thousands of simulated days. This numerical study, while not exhaustive in all parts of parameter space, provides a reasonably good qualitative picture of model behavior in certain regions of this space; these regions are either physically most realistic or else are relevant to completing the global knowledge of possible types of behavior.

The transition from stable stationary solutions to stable periodic solutions occurs by *supercritical* Hopf bifurcation along most of the boundary of the hatched area in Fig. 8. Inside the hatched area, the stable limit cycles arising at the boundary grow in size and keep their stability for a finite distance in parameter values.

Above the turning line of the first resonance, at $\rho \approx 0.4$ in Fig. 8, there exists a limit cycle arising from the (now unstable) main branch solution *mb1*. This limit cycle, which is stable in a large region of parameter space, has small amplitude throughout, so that the flow pattern associated with it always resembles closely the pattern of the stationary solution *mb1*. Transition from this periodic solution to aperiodic solutions occurs for $\alpha \leqslant 0.07$ along the dash-dotted line in Fig. 8. The aperiodic solutions to the left of this line have much larger amplitude and hence greater variations in flow pattern than the periodic solution manifold from which they arise.

Below the first turning line at $\rho \approx 0.04$, transition from periodic to chaotic behavior occurs much closer to the boundary of stability of stationary solutions. We have presented in LG1 a detailed study of solution behavior in the neighborhood of the triple bifurcation point S. The behavior of solutions along the line $\rho = 0.35$ for $0.16 \leqslant \alpha \leqslant 0.18$ was shown in Fig. 8 of LG1.

Power spectra of the solutions (not shown here) exhibit, for α decreasing, a cascade of period-doubling bifurcations from the originally stable limit cycle (Feigenbaum, 1978). Chaos begins at the accumulation point of the sequence of successive bifurcation values, which is $\alpha \approx 0.1624$. Windows of regular behavior and associated intermittency phenomena are also observed inside the chaotic domain, in agreement with the full period-doubling scenario (Kadanoff, 1983).

On the other hand, direct transition from stationary to chaotic behavior is observed numerically at point S itself, in agreement with the scenario of Shilnikov (1965), investigated also recently by Arneodo *et al.* (1982) and by Gaspard and Nicolis (1983). This transition, which occurs over a very small distance in parameter space, is also localized in phase space: the energy of the deviation in the aperiodic solution from the unstable stationary one does not exceed 15% of the energy of the latter, and the planetary flow regime remains unchanged throughout the transition.

At lower values of α, transition to chaos appears to be more complicated. At $\alpha = 0.05$ day^{-1}, and starting with small values of ρ, the chaotic regime is entered along a branch of stationary solutions with blocking-type flow patterns (see Figs. 6 and 7c). Hopf bifurcation occurs at $\rho \approx 0.123$, leading to a stable limit cycle with initial period of approximately 40 days, and with rapidly increasing amplitude. As ρ increases further, period-doubling bifurcations occur, along with the growth of background noise and with intermittency.

Figure 9 shows, for $\alpha^{-1} = 20$ days and $\rho = 0.149$, the time evolution of one diagnostic flow quantity $D_E(t)$, the distance of the given, aperiodic solution from the stationary blocking solution E (see Fig. 6 and Section 5a for details). Throughout the time-dependent evolution, a nearly recurrent sequence of fixed duration appears over and over again. This sequence, labeled S1 in the figure, is about 140 days long and is not repeated identically from one occurrence to another, due to the presence of a significant amount of spectrally-continuous noise. Still, each occurrence is easily identifiable by the similar evolution of several diagnostic variables. The S1 sequences can succeed each other one or more times (three and five successive appearances in the figure), or be interrupted by other sequences, such as S2 in the figure.

As ρ increases above 0.149, the sequence S1 undergoes period doubling, the noise level increases and

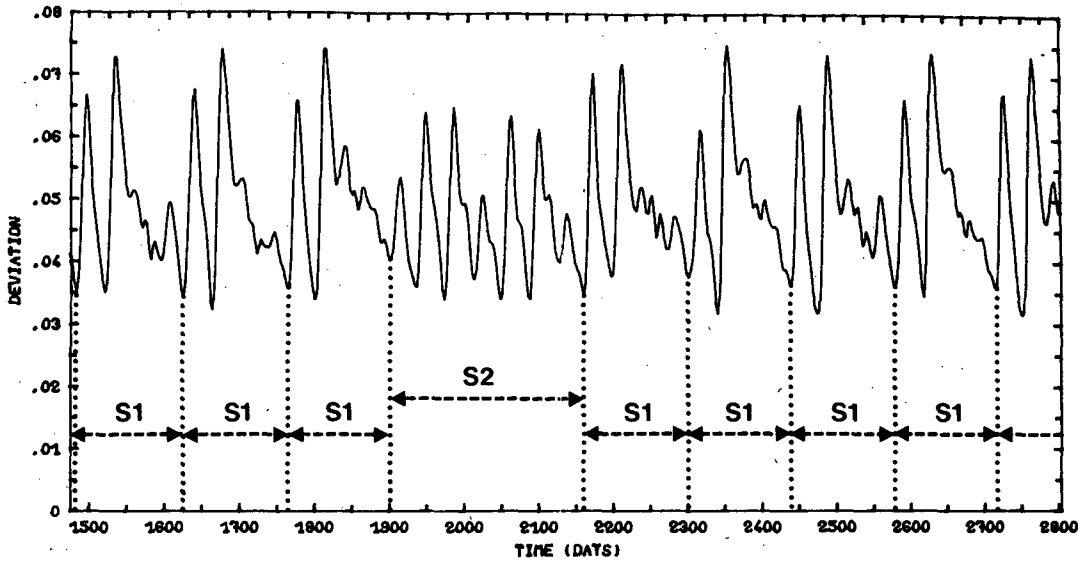

FIG. 9. Time evolution of the deviation D_E from the stationary solution on branch E for $\alpha^{-1} = 20$ days and $\rho = 0.149$. Recurrent sequences are identified by segments marked S1.

more intermittency is observed, i.e., longer separating, nonrecurrent sequences occur. Above $\rho \approx 0.16$, solution behavior seems completely chaotic. Unlike the transitions near point S, significant changes in flow pattern appear for the time evolution represented in Fig. 9.

Inside the chaotic regime which has dash-dotted boundaries in Fig. 8, new instabilities obtain, leading system trajectories to visit new regions in phase space. At this point, the trajectories exhibit sequences of flow patterns associated in succession with different planetary flow regimes familiar to synoptic meteorologists, such as a zonal regime and more meridional regimes (Namias, 1950; Rossby, 1939).

This type of behavior appears to be characteristic of large-scale atmospheric dynamics. Relatively little is known theoretically about transitions between chaotic regimes, or *crises* (Grebogi *et al.*, 1983). To explore the multiplicity of flow regimes which suggest themselves to our attention, we shall study the main features of these regimes numerically, guided by existing theory of phase-space structure on the one hand, and by our synoptic-predictive concerns on the other.

Before doing so, however, it seems at least worth mentioning that an approximate periodicity of 30–50 days has been associated with global fluctuations in the atmosphere's angular momentum (Hide *et al.*, 1980; Krishnamurti and Subrahmanyan, 1982; Madden and Julian, 1971). Oscillations with a period of ~40 days and with a significant barotropic component have also been observed in rotating annulus experiments in the presence of simplified bottom topography with azimuthal wavenumber 2 (J.-C. André, and G. Q. Li, R. L. Pfeffer and R. Kung, personal communications, 1984). The intermittent character of flow sequences (Fig. 9) associated with a continuous spectral component might account for the width of the peak in the spectrum of the observed fluctuations (see also Section 5a and discussion of Fig. 13a there). For a more precise interpretation of our barotropic model's results in terms of naturally occurring, mixed barotropic and baroclinic phenomena we refer to Section 6.

5. Persistence and predictability

a. Persistent regimes

We study here the existence of recurrent, persistent flow-pattern sequences in the evolution of chaotic solutions. The closest analogy between such persistent sequences and actual planetary flow regimes is obtained in our model for the region of the second resonance, at relatively small values of α. Therefore, we shall investigate the question of persistent flow patterns for the parameter domain shown in Fig. 6 and indicated by a two-sided arrow in Fig. 8: $0.13 \leq \rho \leq 0.35$, with $\alpha = 0.05$ day^{-1} and $h_0 = 0.1$. In this domain, the only stable stationary solutions lie on the isola, and most numerically observed solutions are aperiodic.

As a measure of persistence, we adopt the quantity $C(t)$,

$$C(t) = \frac{\|\Psi(t+\tau) - \Psi(t)\|}{\tau}, \qquad (11)$$

which measures the speed of the solution point $\Psi(t)$ along its orbit in phase space. Here τ is a sampling

time interval, taken equal to two days in dimensional units, and the numerator equals the root-mean-square difference between the two successive stream function fields (see also paragraphs following Eqs. (9) and (10) for the definition and use of $\|\cdot\|$). When $C(t)$ is small for a given length of time, the evolution of the flow pattern in physical space is observed to be slow, and the pattern persists for that length of time.

Figures 10a–e show the evolution of $C(t)$ for several solutions computed at $\rho = \rho_1, \rho_2, \cdots, \rho_5$, with ρ increasing from Fig. 10a to Fig. 10e, as indicated in the caption (see also Fig. 6 for orientation). Notice first that the total range of variation in $C(t)$ increases from $\Delta C \approx 0.10$ in Fig. 10a to $\Delta C \approx 0.50$ in Fig. 10e. Hence the irregularity of the motion in phase space increases with ρ.

The minima of $C(t)$ are not as sharp as the maxima. The width of the minima is larger and their flatness more pronounced for larger values of ρ, both width and flatness being most striking for $\rho = \rho_4$. It turns out that all persistent sequences belong to the blocking family of flow patterns for $\rho = \rho_1$ and $\rho = \rho_2$. They have exclusively zonal patterns for $\rho = \rho_4$ and $\rho = \rho_5$. Persistent sequences with either pattern are present for the intermediate value $\rho = \rho_3$.

A more precise definition of persistence can be given by choosing an offset value C_0. Averaging the flow patterns during a given sequence where $C(t)$ remains below the offset, $C(t) \leqslant C_0$, produces a *composite pattern*. Such a composite is shown in Fig. 11a for numerical experiment 2 at $\rho = \rho_2$ and the sequence centered at $t = 2640$ days with an offset value $C_0 = 0.0045$. It possesses strong similarities to the stationary blocking solution shown in Fig. 7c. All other composites obtained in this experiment are very close to the one shown. The same results hold for experiment 1 at $\rho = \rho_1$.

In both experiments 1 and 2, two consecutive sequences are separated by rather complicated episodes. Most of these episodes possess zonal transients. One of them, marked by an arrow in Fig. 10b, is shown in Fig. 11b. These transients, however do not bear any similarity with the Zonal 1 family, since they remain at low energy.

We must mention here two points which will be developed later. First, all along the two experiments at $\rho = \rho_1$ and $\rho = \rho_2$, the time-evolving solution remains closer to the blocked branch of stationary solutions than to Zonal 1 or Zonal 2-type solutions. Second, Zonal 1-type solutions are seldom observed numerically in the parameter range where they exist as stable stationary solutions. The basin of attraction of this branch appears to be very small in volume and limited to the immediate vicinity of the branch in distance. We shall see how this feature is modified by changing the deformation radius λ.

The Double-Block type of solution is also hardly apparent in time-dependent model behavior. The numerical experiment just discussed, at $\rho = \rho_2$, had initial data close to such an unstable stationary solution, but never returned there.

The persistence behavior in Fig. 10d, e is rather different from Fig. 10a, b. The minima of $C(t)$ are quite flat compared to the maxima, thus defining sequences of very persistent flow patterns. But sharp instability peaks are in evidence, showing that the solution-point in phase space is violently expelled from the region of persistence. It then relaxes slowly to a quieter evolution, producing a reversed, irregular sawtooth profile in the $C(t)$ time series. Furthermore, the observed flow characteristics are reversed with respect to the previous experiments 1 and 2; persistent sequences show zonal patterns and transient blocks occur during episodes of rapid flow evolution, together with other complicated types of highly meridional circulations.

This succession of events is strongly reminiscent of the description given by Namias (1950) of an individual "index cycle." During such a cycle, high-index flow with strong midlatitude westerlies and long superimposed waves is followed by a shortening of the upper-air wavelength pattern, then by a sudden and complete breakup of the westerly flow into north–south oriented pressure cells, with occlusion of stationary cyclones and strong anticyclogenesis, and finally by a gradual reestablishment of the zonal flow. The low-index portion of the cycle, where meridional flow is strong, includes blocking patterns, but their duration varies between a few days and a few weeks.

The whole sequence of events is called a cycle because a high-index pattern occurs at its beginning as well as at its end; however, no exact periodicity, i.e., no constant duration of the cycle, is implied by Namias or by any other observations. Furthermore, the occurrence of marked cycles is favored at certain seasons, but is not the same from year to year, suggesting a dependence on thermal forcing; such forcing is represented in our model by the parameter ρ.

To study in further detail the character of flow patterns in our model for this index-cycle-like evolution, we composited persistent sequences as before. Figure 12a shows one composite pattern obtained from the sequence centered at $t = 2330$ days in Fig. 10e with the offset value $C_0 = 0.009$. This value of C_0 is equivalent to the one used in experiment 2, at $\rho = \rho_2$, after normalization by the mean value of $C(t)$ in either experiment.

Surprisingly, this composite is more similar to the Zonal 1 type of solution, which does not exist as a stationary solution at this value of parameters, than to the stationary solution on the Zonal 2 branch at $\rho = \rho_5$. The same observation holds for all composites obtained from experiment 4. In experiment 5, on the other hand, some composites are found to be closer to Zonal 2 stationary solutions.

One transient solution, marked by the right-pointing arrow in Fig. 10e, is shown in Fig. 12b. This dipole

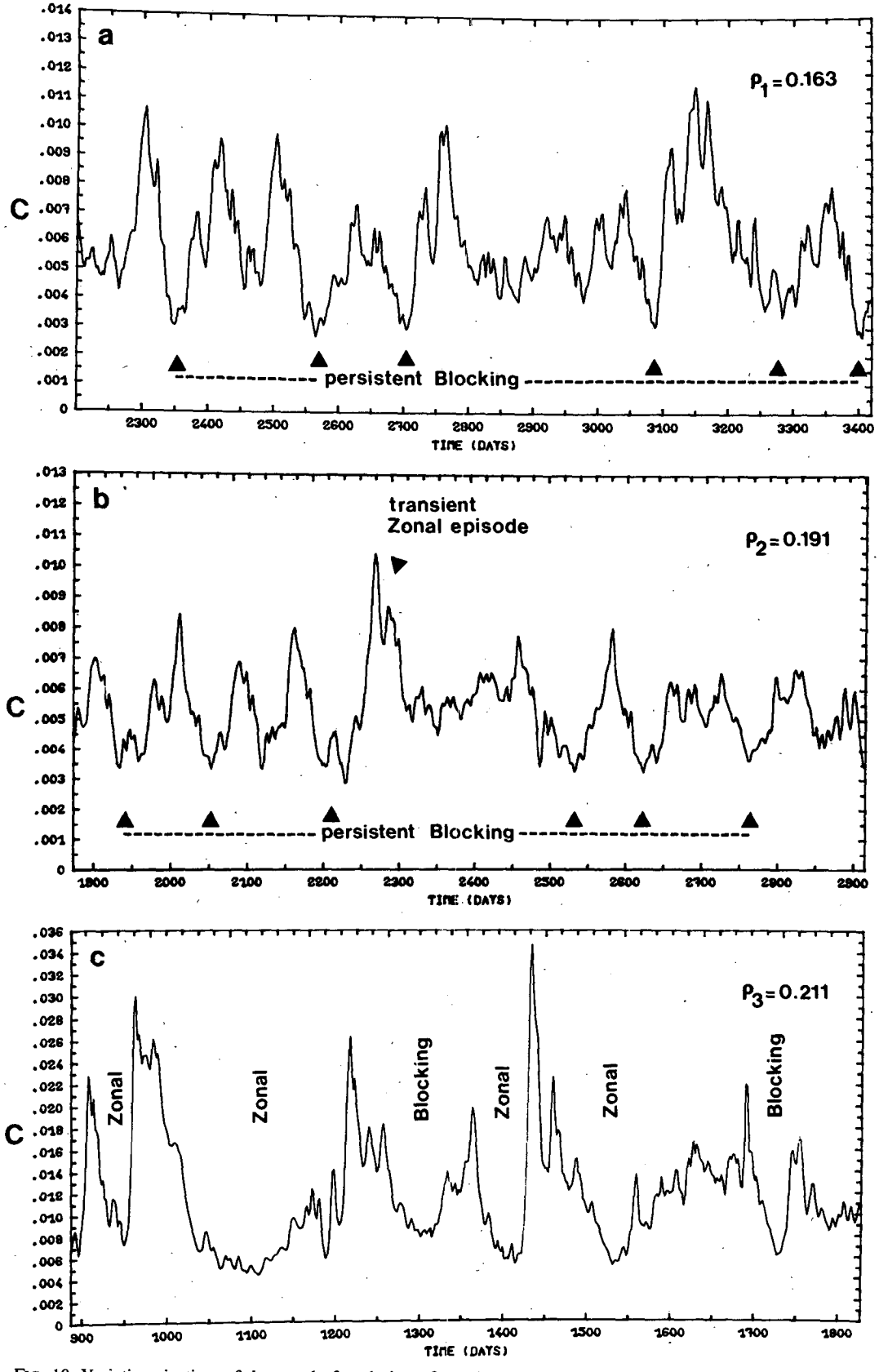

FIG. 10. Variations in time of the speed of evolution of solutions $C(t)$, Eq. (11). (a) $\rho_1 = 0.163$, (b) $\rho_2 = 0.191$, (c) $\rho_3 = 0.211$, (d) $\rho_4 = 0.228$, (e) $\rho_5 = 0.272$. Persistent sequences correspond to low values of C. These sequences, their synoptic nature, as well as some transients, are indicated in the figure.

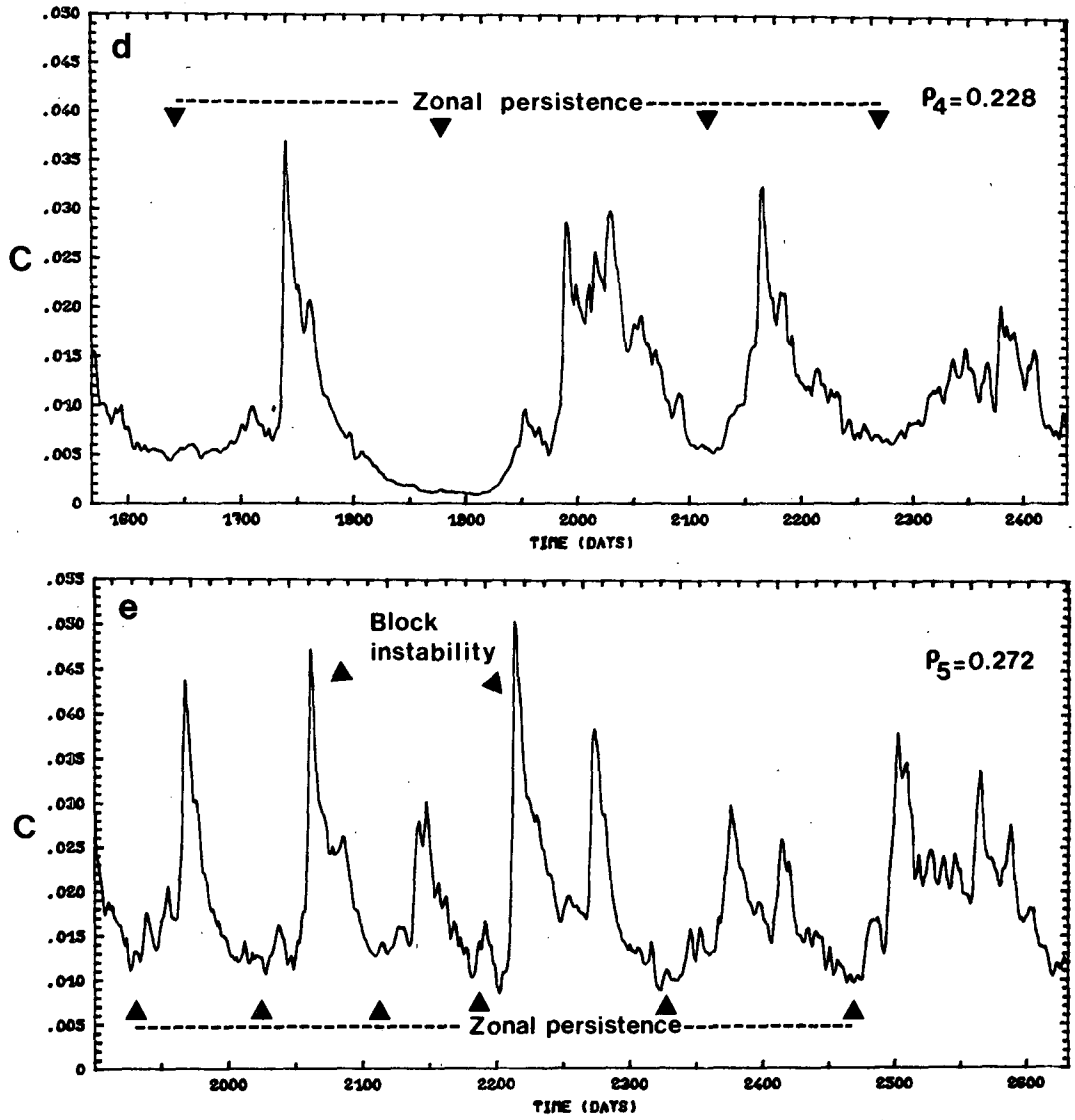

FIG. 10 (*Continued*)

block resembles the modon pattern studied by McWilliams (1980) in an atmospheric context. In our model, it appears only as a very transient, unstable flow pattern. But the question of stability of isolated local structures in realistic large-scale flows is under active investigation (Leith, 1984; Malanotte-Rizzoli, 1982; Pierrehumbert and Malguzzi, 1984), and the interplay between the two points of view, local and global in physical space, will certainly contribute greatly to a better understanding of the question of atmospheric persistent anomalies. Notice in fact that blocking events with a similar structure are sometimes quite short-lived (Sumner, 1954).

The intermediate experiment 3 (Fig. 10c) exhibits both types of persistent sequences, zonal and blocked. The flow pattern characteristic of each sequence, easily identifiable by visual inspection of microfilm output (not reproduced here), is indicated in Fig. 10c. Four zonal sequences and two blocking sequences appear in the numerical solution segment displayed in the figure, but the relative frequency and length of the sequences depends on the exact value of ρ and on the segment of aperiodic solution chosen.

The persistent sequences discussed here, like the stationary solutions they resemble (Section 3c), exhibit easterlies in low latitudes. For persistent zonal flow, at $\rho = \rho_5$, the maximum easterly speed at the equator is 8 m s^{-1}, while the maximum westerly speed is 50 m s^{-1} at 60°N and zonal flow is nearly null between 7 and 20°N. For persistent blocked flow, at $\rho = \rho_2$, the maximum easterlies are 3 m s^{-1}, the maximum westerlies 25 m s^{-1}, and a more sharply defined

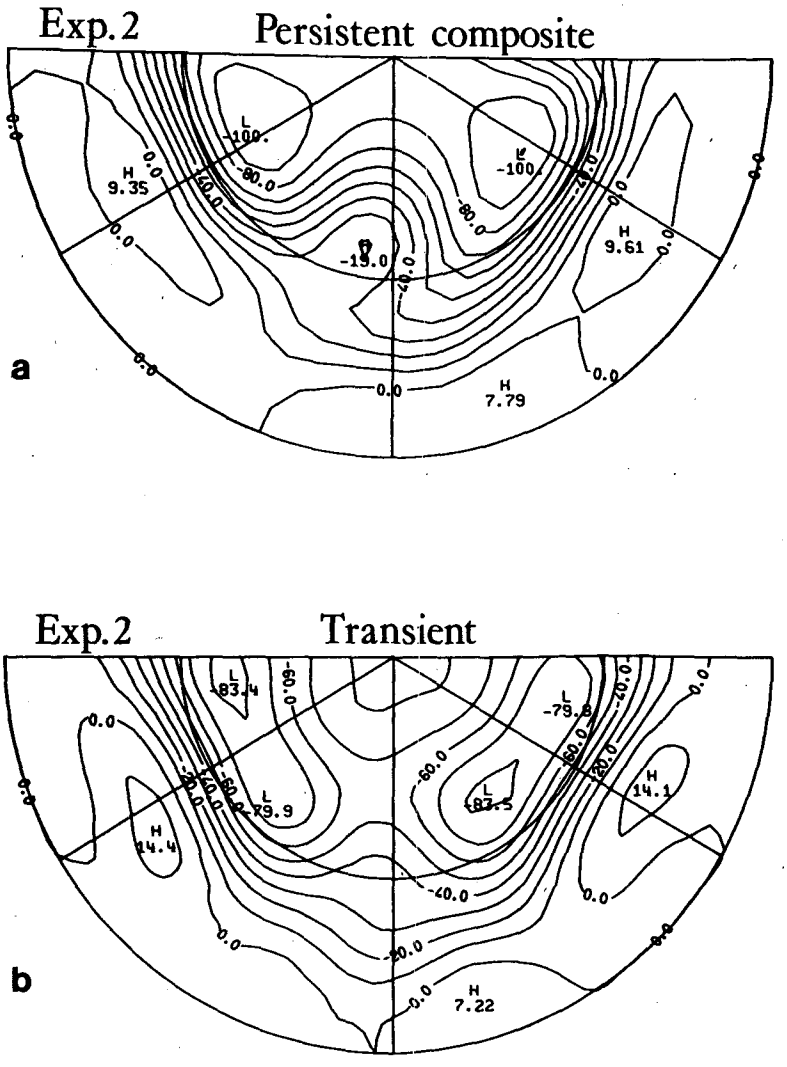

FIG. 11. Two streamfunction fields from experiment 2 at $\rho_2 = 0.191$: (a) composite of the persistent sequence centered at $t = 2640$ days in Fig. 10b, based on an offset value $C_0 = 0.0045$; (b) instantaneous field taken during the transient Zonal episode labeled in Fig. 10b.

critical belt of near-zero mean zonal wind speed occurs near 10°N.

In general, the critical line of null zonal wind speed is ill-defined. Its latitudinal position changes with a characteristic time comparable to that of all other changes in low wavenumbers, more slowly in a blocked regime and faster in a zonal regime. The distribution of zonal momentum with latitude in the model changes in qualitative agreement with observed changes between high-index and low-index situations (Namias, 1950). But the profiles of mean zonal wind are not good indicators, by themselves, of transitions between persistent episodes and more transient ones.

We have seen in Figs. 10–12 that persistent sequences of flow patterns exist and that their composites tend to resemble certain stationary solutions, which are unstable for the given parameter values. This suggests an important role for such unstable solutions in the flow dynamics (see also Section 4a). In order to check more directly the connection between persistent sequences and stationary solutions, we computed for all experiments the deviations $D_i(t) = \|\Psi(t) - \Psi_i\|$ to a prescribed stationary solution Ψ_i. Each label i corresponds to one particular branch of stationary solutions as indicated in Figs. 6 and 13. For each experiment at a given value of ρ, we consider stationary solutions present at this value of ρ. An exception is made for Zonal 1 type solutions: for values of ρ where this branch does not exist, we consider the solution located at the nearest turning point of the isolated branch, marked by a star in Fig. 6. The correlation coefficient between the pair of time

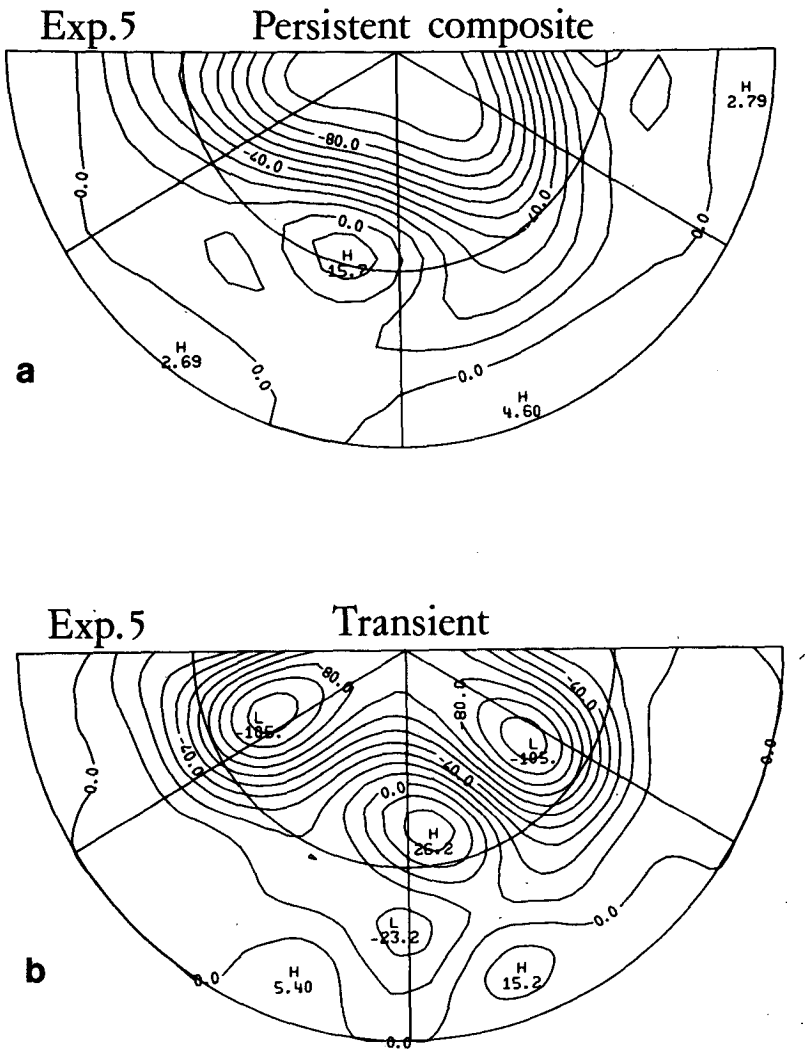

FIG. 12. Streamfunction fields from experiment 5 at $\rho_5 = 0.272$: (a) composite of the persistent sequence centered at $t = 2330$ days in Fig. 10e with an offset value $C_0 = 0.009$; (b) instantaneous snapshot taken during the transient Block instability at $t = 2220$ days in Fig. 10e.

series $C(t)$ and $D_i(t)$ is also computed and indicated in Fig. 13.

Figure 13a shows the variations of $D_i(t)$ for experiment 2 at $\rho = \rho_2$. The trajectory remains close to both blocked branches D and E, with some preference for branch E. Larger distances are maintained to the Double-Block solution (F), Zonal 2 solution (C) and to the Zonal 1 point closest to the solution (B). A general modulation of period close to 40 days contains a significant part of the autocorrelation power spectrum (not shown here) of all deviation time series, $D_i(t)$. This modulation is reminiscent of the original limit cycle which develops along the blocked branch D when it loses its stability at lower ρ (see also end of Section 4b and Fig. 9).

The deviations from branches B, C and F are poorly correlated with $C(t)$. There is better correlation with blocked branches D and E, although not as good as expected from persistent composite patterns and examination of the detailed microfiche film of the experiment. The reason for this imperfect correlation is that our measure of deviation $D_i(t)$ does not distinguish between phase displacements of a given synoptic pattern and actual change in pattern. Essentially the same results with respect to $D_i(t)$ and correlation with $C(t)$ hold for experiment 1 (not shown here).

Figure 13c shows the variations of $D_i(t)$ for experiment 4. The trajectory is now closest to the Zonal 1 (B) and Zonal 2 stationary solutions (C), while the blocked solution (E) remains at larger distances. The deviation from the Zonal 1 solution is strongly correlated with $C(t)$; cf. Fig. 10d. The weaker, but still apparent correlation with deviation from the Zonal

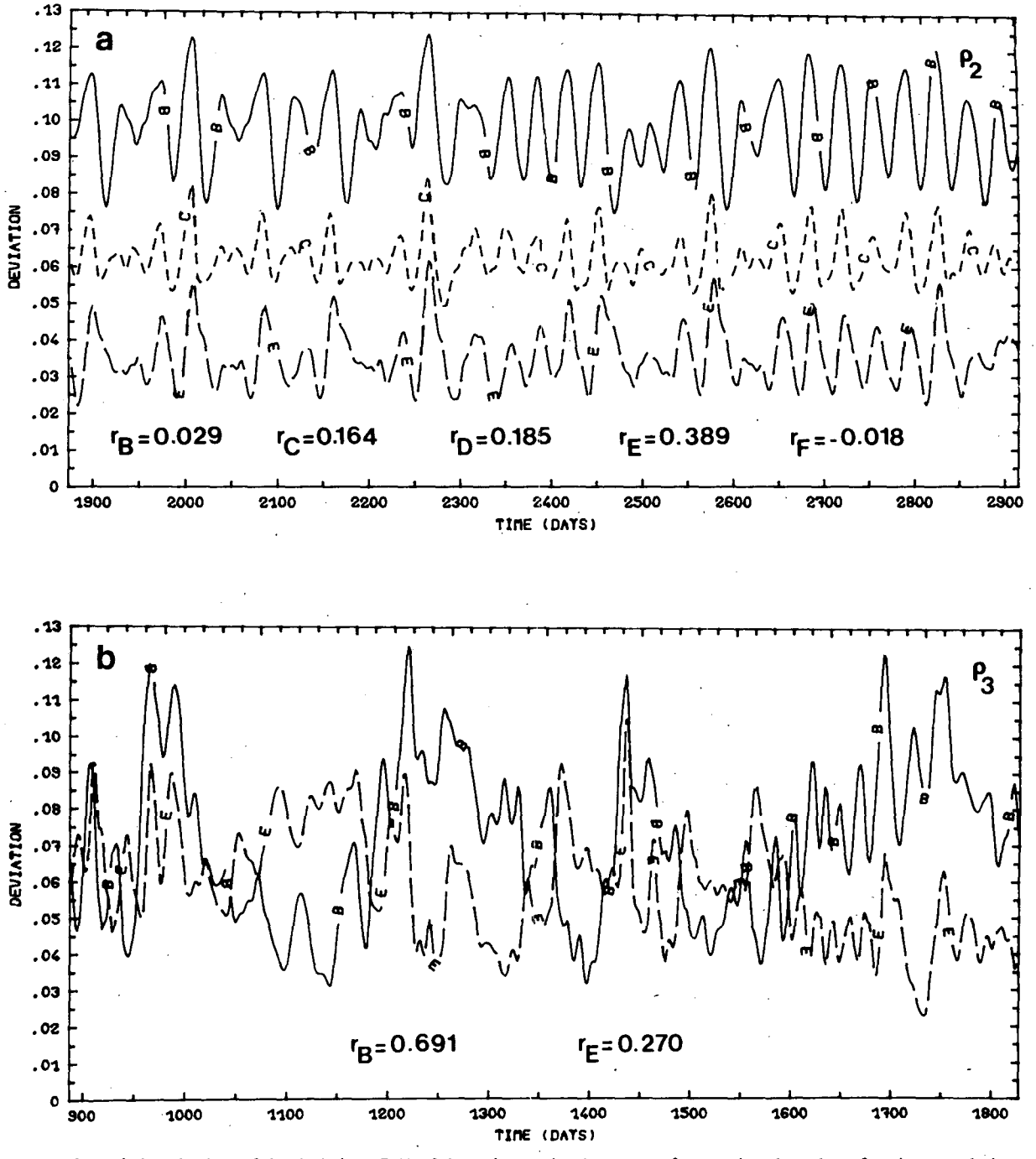

FIG. 13. Variations in time of the deviations $D_i(t)$ of the trajectory in phase space from various branches of stationary solutions. Subscripts i = A, B, C, D, E refer to the branch labels in Fig. 6. In order to improve legibility, each label is associated with a specific line pattern: B, solid; C, short dashes; D, long and short dashes; E, long dashes. The correlation r_i between the time series $C(t)$ and the deviations $D_i(t)$ is indicated on each panel. For experiments 3 to 5, the deviation D_B is taken with respect to the saddle-node bifurcation point of the isolated Zonal 1 branch indicated by a star in Fig. 6. (a) Experiment 2 at ρ_2 = 0.191, deviations from branches B, C and E, (b) Experiment 3 at ρ_3 = 0.211, deviations from B and E branches, (c) Experiment 4 at ρ_4 = 0.228, deviations from B, C and E branches, (d) Experiment 5 at ρ_5 = 0.272, deviations from B and C branches.

2 branch comes entirely from episodes of rapid variations, during which the trajectory is actually far from any stationary solution. The deviation from the blocked branch (E) is now clearly anticorrelated with $C(t)$ during persistent sequences. However the overall correlation between $D_E(t)$ and $C(t)$ is close to zero due to the positive contribution of transients.

For experiment 5 (Fig. 13d) the average deviations

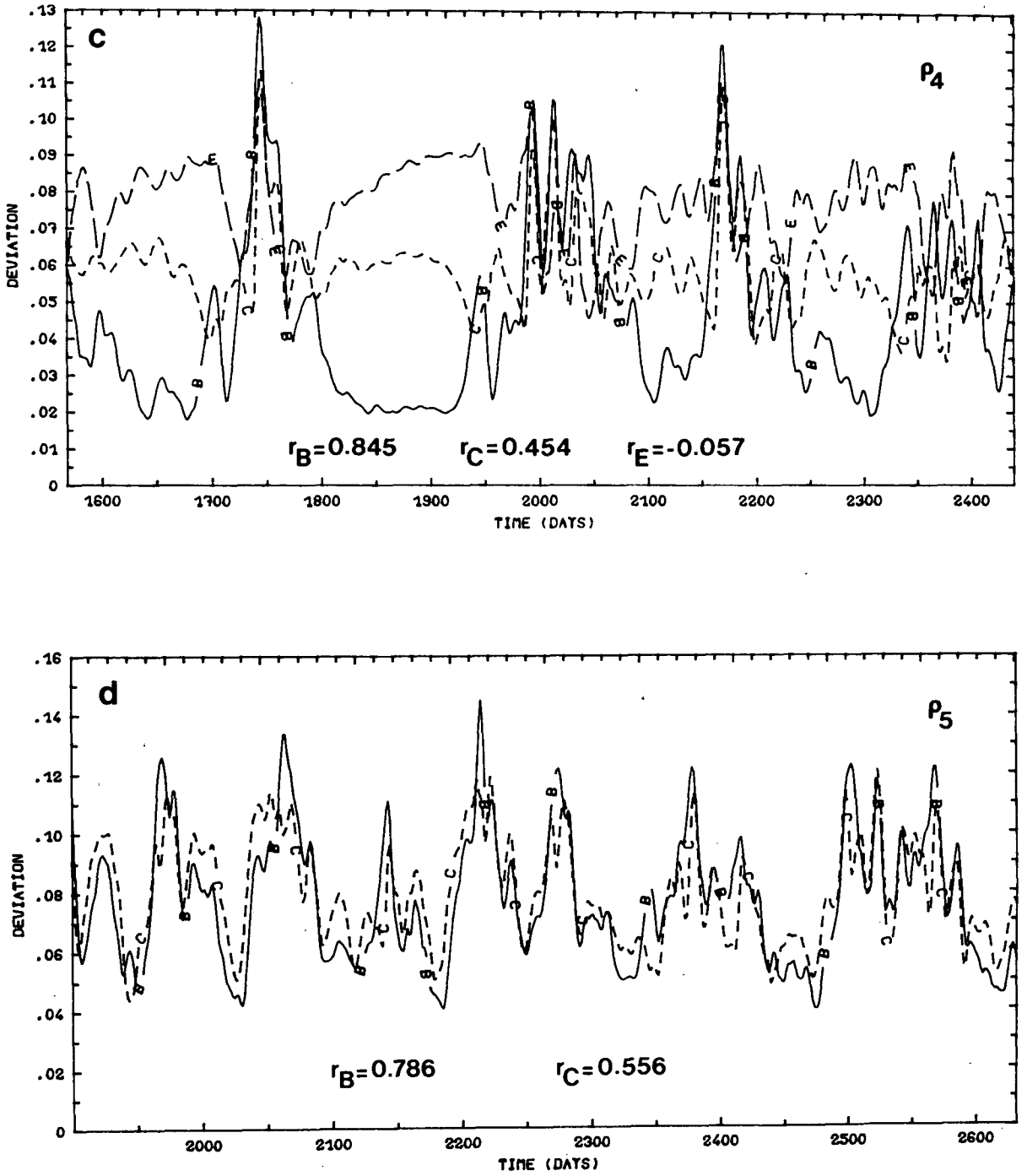

FIG. 13 (*Continued*)

from stationary solutions increase. The correlation between $C(t)$ and the deviation $D_B(t)$ from Zonal 1 solutions is very good (see also Fig. 10e), and remains higher than between $C(t)$ and the deviation $D_C(t)$ from the Zonal 2 solution. However, $D_C(t)$ is also well correlated now with $C(t)$. There is still no correlation between $C(t)$ and deviations from the blocking branch (not shown here). As ρ increases beyond ρ_5, the deviations from the Zonal 1 and Zonal 2 branches tend to correlate equally well with $C(t)$, until new weather regimes appear due to the CDV resonance.

Finally, for experiment 3 (Fig. 13b), the analysis of deviations $D_i(t)$ confirms our previous observations. The minima of deviation from Zonal 1 solutions are well correlated with minima in $C(t)$ during episodes designated zonal in Fig. 10c, while persistent sequences

of blocking, as indicated in Fig. 10c, are associated with closer proximity to the blocked branch of stationary solutions (E). The overall correlation is better between $D_B(t)$ and $C(t)$ than between $D_E(t)$ and $C(t)$, being again a function of the exact value of ρ and of solution segment.

For all zonal regimes, we have seen that the Zonal 1 type of solution plays a very special role in attracting the trajectories into its neighborhood. On the other hand, there is an apparent paradox in the fact that Zonal 1 regimes are observed for parameter values for which Zonal 1 stationary solutions do not exist, while blocking regimes obtain when Zonal 1 solutions do exist. A few qualitative arguments may help us understand, at least roughly, this behavior.

The first part of the paradox is probably a consequence of the saddle-node bifurcation, which terminates the isolated branch of Zonal 1 stationary solutions at ρ just below $\rho_3 = 0.211$. In such a bifurcation, illustrated in Fig. 14 (see also Ghil, 1976, his Fig. 7), two stationary solutions, one stable, the other one unstable, coalesce and leave behind an arc of one-dimensional manifold along which the motion in phase space is slow (null at the bifurcation point itself) compared to the rapid convergence onto this arc from other directions.

This topological structure traps the trajectory along the slow manifold, leading to persistent sequences of Zonal 1-like flow patterns. However, the efficiency of this mechanism to generate such sequences depends on the ability of the entrance funnel into the neighborhood of the given arc to span a large portion of phase space, in order to ensure recurrence of the phenomenon. Further consequences of the action of this mechanism on the model's predictability properties are presented in the next subsection.

The explanation of the paradox's second part is somewhat more complex. In addition to the two saddle-node bifurcation points at its ρ-extremities, several Hopf bifurcations from the branch of Zonal 1 solutions occur along the most energetic, upper part of the isola; the number of unstable eigenvalues

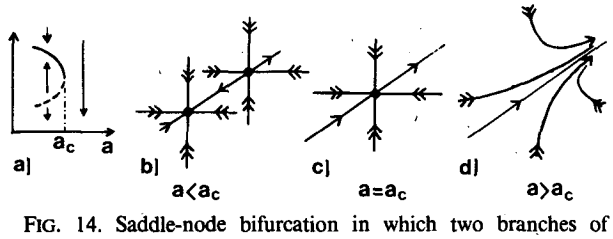

FIG. 14. Saddle-node bifurcation in which two branches of stationary solutions, one stable and the other unstable, coalesce at the parameter value $a = a_c$. For $a < a_c$, the flow in phase space close to the pair of stationary solutions looks as it appears in panel (b), with rapid contraction in the two transversal directions symbolized by double arrows. At $a = a_c$ (c), a neutrally stable point obtains when the previous two fixed points merge. For $a > a_c$ (d), slow motion occurs along the "ghost" of the orbit previously connecting the two fixed points, with rapid transversal contraction resulting in a funneling effect.

for $\mathcal{L}_s$ varies there from 0 to 4. At least one of the Hopf bifurcations is *subcritical*, leading to an unstable limit cycle which surrounds the stable solution when it exists and repels most of the incident trajectories (compare Ghil and Tavantzis, 1983, their Figs. 7a and 9f). This may explain the smallness of the attracting basin for stable Zonal 1 stationary solutions and the nonexistence of stable attractors like limit cycles in the vicinity of the entire isolated branch.

On the other hand, there exists numerically for $\rho \leqslant 0.205$ a stable attractor associated with the blocking-type branches of stationary solutions. Almost all trajectories converge rapidly to this attractor, so that no return is observed to the Zonal 1 branch. In the neighborhood of $\rho \approx 0.205$, a complicated transition occurs, after which the preceding attractor loses its stability and trajectories are allowed to return recurrently close to the Zonal 1 branch. Arneodo *et al.* (1982) suggest a possible link between such transitions and the existence of heteroclinic orbits connecting the different branches of stationary solutions.

Several results seem to corroborate this hypothesis. We show for instance in Fig. 15 the evolution at $\rho = 0.204$ of deviations $D_B(t)$ from the Zonal 1 stationary solution, starting from the neighborhood of the stable upper branch of the isola. Instead of going directly to the stable zonal solution nearby, the trajectory is first ejected to a large distance, displaying an episode of transient block, which is out of phase with the unstable stationary blocking solution; only after this large excursion does the trajectory return to the stable zonal solution near its starting point. Since heteroclinic orbits are structurally unstable, it is difficult to provide further numerical evidence for their existence and a detailed analytic study would be required.

Previous results are sensitive to the value of the Rossby radius of deformation L_R. Although L_R has no effect on the distribution of stationary solutions, it influences their stability and the dynamics of time-dependent solutions. A small value of L_R favors the excitation of a large-scale stationary response to orographic forcing, like blocking, since it reduces the phase speed of planetary waves.

On the other hand, we may expect for $L_R = \infty$ to observe a more zonal circulation. This is actually the case: the Zonal 1 branch of stationary solutions is then globally attracting. Throughout the domain of existence of this branch, all trajectories end up on it or on a stable limit cycle in its close vicinity.

No permanent blocking regime has been numerically observed for $L_R = \infty$ except at small values of ρ close to the first Hopf bifurcation. However, a metastable blocking regime persists in certain parameter ranges for a very long time; in practice this is equivalent to the coexistence of multiple regimes. The situation is illustrated below.

Figure 16 shows the time evolution of the deviations from stationary solutions for $\rho = \rho_3$ and $L_R = \infty$.

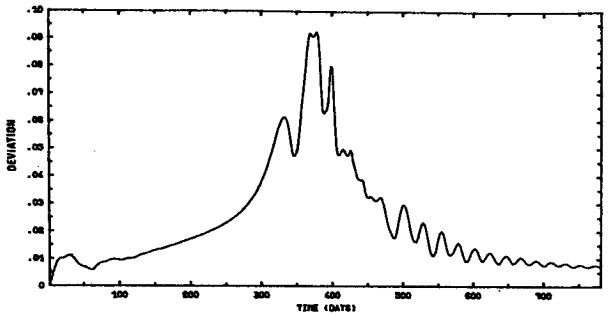

FIG. 15. Time evolution of the deviation D_B for an experiment at α^{-1} = 20 days and ρ = 0.204, started in the vicinity of branch B.

Initial data were taken in a blocking regime from the previously shown experiment for $\rho = \rho_3$ and L_R = 1100 km. This regime persists for 1500 days, after which the flow follows a stable limit cycle of large amplitude with strong persistence in a Zonal 1 regime and a sequence of rapid evolutions which span Zonal 2 and Blocking solutions. Here again, the existence of a heteroclinic connection for a nearby parameter value is strongly suggested. At higher values of ρ, only zonal regimes obtain, with flow patterns between Zonal 1 and Zonal 2. Pure Zonal 2 regimes are also observed for some values of ρ.

b. *Regime-dependent predictability*

So far, we have seen the connection between the persistence of certain flow patterns in physical space and the proximity of the trajectory in phase space to stable or unstable stationary solutions with similar flow patterns. We now investigate the potential usefulness of this connection in determining the predictability of the associated planetary flow regimes.

This first leads us to examine the statistics of persistent sequences in the numerical experiments described above. Figure 17 shows the number of events per simulated year plotted against the duration of events, for solutions computed at $\rho = \rho_1, \rho_2, \cdots, \rho_5$. In order to obtain a sufficiently high confidence level, long-time integrations were performed over time intervals 24 times as long as those displayed in Figs. 10a–e. For ρ = 0.20, this corresponds to roughly 65 years of dimensional time, a record over four times as long as the 15-year data set at the basis of current observational studies (Blackmon *et al.*, 1979; Dole and Gordon, 1983; Shukla and Mo, 1983), and used here for each separate experiment. The sampling interval is 1.5 nondimensional time units, or three days at ρ = 0.20.

The offset value for each experiment is taken as the time average of $C(t)$ minus one-half of its standard deviation. This choice of offset means that we compare here properties of persistence relative to the prevailing regime imposed by the parameter values. It is clear from Fig. 10, and was mentioned already in Sec. 5a, that flow evolution in the blocking-dominated parameter range of $\rho_1 \leqslant \rho \leqslant \rho_2$ is on the average much more persistent than in the zonal-flow dominated range $\rho_4 \leqslant \rho \leqslant \rho_5$. Nevertheless, the minima and maxima of $C(t; \rho)$ for given ρ still correspond to persistent and rapidly changing flow patterns, respectively.

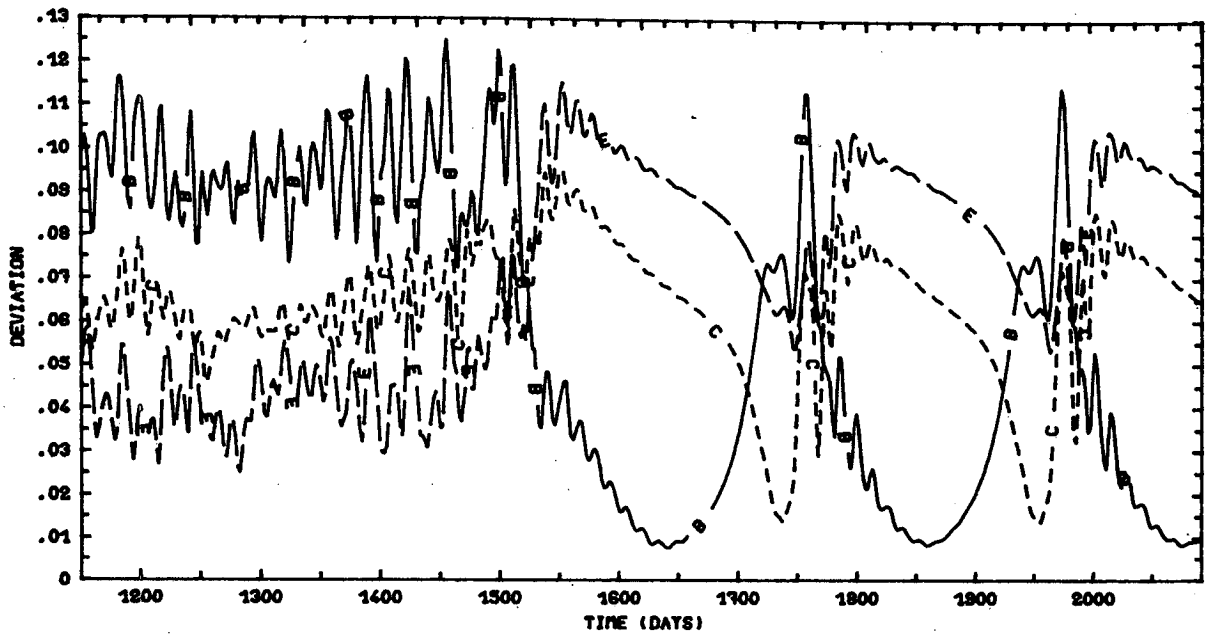

FIG. 16. Time evolution of deviations from the B, C and E branches for an experiment at α^{-1} = 20 days and ρ = 0.211 with $L_R = \infty$.

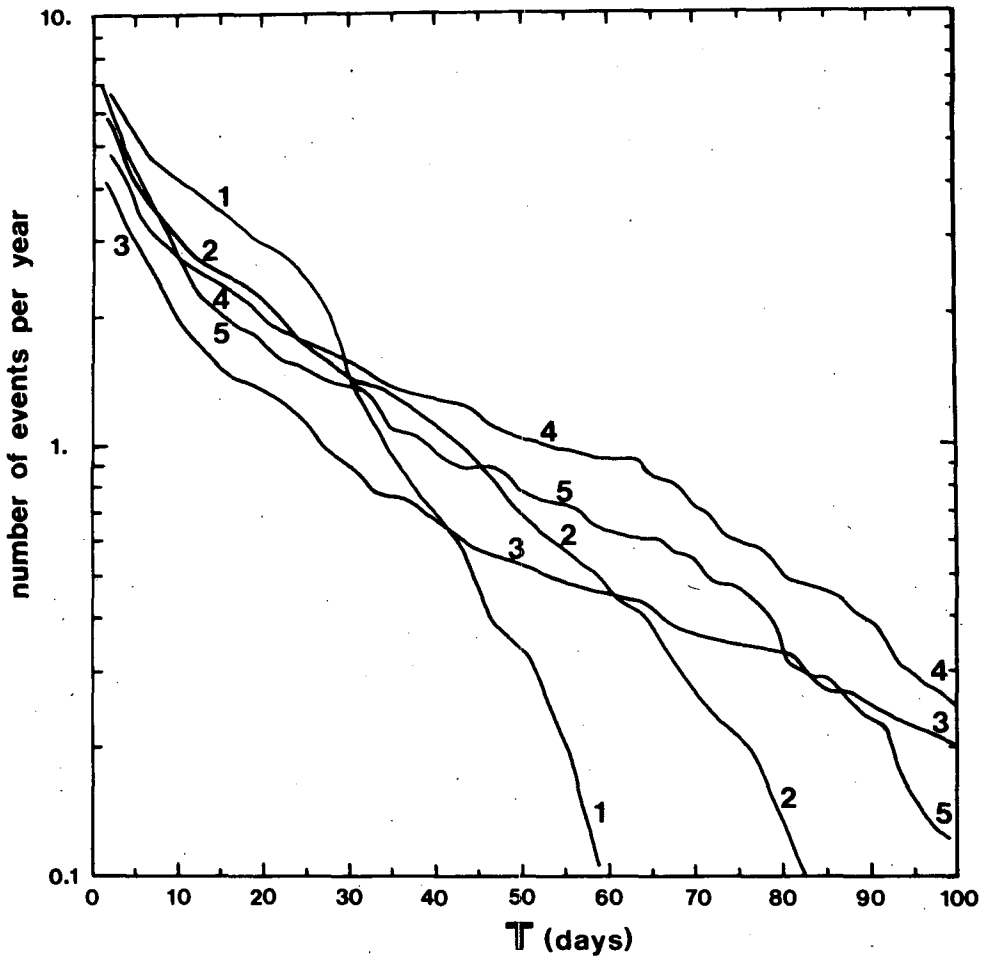

FIG. 17. Number of persistent sequences per year whose duration exceeds the number of days indicated on the abscissa, for extended experiments 1 to 5. The offset value for persistence C_0 is taken for each experiment as the average of C minus one-half of its standard deviation: $C_{01} = 5.0 \times 10^{-3}$, $C_{02} = 5.0 \times 10^{-3}$, $C_{03} = 7.0 \times 10^{-3}$, $C_{04} = 8.8 \times 10^{-3}$, $C_{05} = 12.6 \times 10^{-3}$. Each curve is labeled with the number of the corresponding experiment.

All curves in Fig. 17 exhibit a smooth decrease in the number of persistent sequences with the duration of persistence. The lack of a maximum, or even of a pronounced plateau at a given duration, indicates that neither zonally-dominated sequences, $\rho_4 \leqslant \rho \leqslant \rho_5$, nor blocking-dominated sequences, $\rho_1 \leqslant \rho \leqslant \rho_2$, have a preferred duration.

In the log-linear coordinates of the figure, the duration of runs, or persistence of a given sign for a linear first-order Markov process with mean zero, is given by a straight line. The slope $-\nu$ of such a line indicates the exponential relaxation time or e-folding time τ of the process, often called *red noise* for short, with $\tau = 1/\nu$. We have fitted a straight line by least squares to the curves in Fig. 17, ignoring the first few points where uncertainty is due to the finite sampling interval, and the last few which are uncertain due to the finite length of each experiment. The results are shown in Table 1.

The exact values of τ vary somewhat with the offset criterion chosen, but the relative ordering $\tau_1 < \tau_2 < \tau_4 < \tau_5$ is always the same. This shows in fact longer persistence times for zonal sequences than for blocking sequences.

TABLE 1. The characteristic exponent λ_L, its inverse λ_L^{-1}, and the e-folding time τ for experiments 1 through 5.*

	Experiment				
	1	2	3	4	5
ρ	0.149	0.191	0.211	0.228	0.272
λ_L (day^{-1})	0.028	0.033	0.058	0.087	0.095
λ_L^{-1} (day)	36	30	17	11	10
τ	14	25		42	47

* The estimated precision of λ_L is ±5%, based on using different initial data and different segments of the same orbit (compare Grebogi *et al.*, 1983).

It is interesting to compare these results with Fig. 8 of Dole and Gordon (1983). They present the same type of statistics for regional anomalies of 500 mb geopotential fields from 15 winters of Northern Hemisphere atmospheric data. The general character of the curves is very similar. Positive anomalies of a given duration occur more frequently than negative ones in both PAC and ATL regions, as defined by Dole and Gordon, with PAC positive being most persistent of all. The synoptic character of the flow across the continental margin for PAC positive and ATL negative anomalies is zonal, being blocked for PAC negative and ATL positive.

Thus we obtain reasonable qualitative agreement with atmospheric behavior as described by Dole and Gordon (1983). The actual values of τ for our model are considerably higher than those reported from observations. This discrepancy is most likely due to the limited resolution and absence of baroclinic transition mechanisms between regimes in our model, and we shall return to this problem in the concluding remarks, where related results of Reinhold and Pierrehumbert (1982) will also be discussed.

Curves 1 and 2 deviate actually from a straight line by being convex, except near the origin, while 4 and 5 are rather concave up to very high persistences. More precisely, one can define separately the least-square slope of each curve for durations between 5 and 30 days, $\nu_j^{(1)}$, and between 35 and 60 days, $\nu_j^{(2)}$. The corresponding slopes satisfy the inequalities $\nu_j^{(1)} < \nu_j < \nu_j^{(2)}$ for blocked regimes, $j = 1$ and 2, and the opposite inequalities for zonal regimes, $\nu_j^{(1)} > \nu_j > \nu_j^{(2)}$ for $j = 4$ and 5. Thus for instance $\tau_2^{(1)} = 35$ days, $\tau_2 = 25$ days (see Table 1), and $\tau_2^{(2)} = 20$ days, where $\tau_j^{(k)} = 1/\nu_j^{(k)}$.

The curve for experiment 3, at the transition between zonal-flow dominated and blocked-flow dominated regimes in parameter space, is more complex. This is due to the fact that each of the two coexisting regimes actually has a different characteristic distribution of persistence times, with distinct means and hence distinct threshold values. Curve 3 is thus the weighted superposition of two separate curves (not shown), and no single, well-defined value of τ_3 exists.

The deterministic dynamics of our model thus produce waiting times for exit from a given flow regime which have an approximately exponential distribution, i.e., linear in semilogarithmic coordinates. For a pure, linear red-noise process, this distribution is exactly log-linear and its slope gives the probability of continued persistence of the given flow pattern, with the probability of exit being proportional to the absolute value of the slope ν.

We suspect, therefore, that the local slope of the distribution in our nonlinear, deterministic model is also proportional to the probability of exit from a given flow regime for persistent sequences of given length. These considerations suggest introducing the concept of *regime predictability* of a flow pattern, in model and nature. This concept depends on the persistence properties of a finite region of phase space, be it an isolated attractor set, coexisting with other attractors, or a subset of an attractor which is only weakly connected to other portions of the attractor, and which is close to an unstable fixed point.

Regime predictability must be distinguished from the more familiar concept of *pointwise predictability,* which arises from the growth of small errors, at each point in physical space or in phase space, and at each moment in time. Pointwise predictability can be estimated by computing the mean rate of divergence of two trajectories starting close to each other in phase space. Predictability studies of the atmosphere by the three distinct methods of i) naturally-occurring analogs, ii) the statistical theory of turbulence and iii) numerical experiments with general circulation models (Lorenz, 1984) all show that small errors, on the average, grow exponentially. This fact is in agreement with the results of dynamical system theory.

The exponential growth of small errors in a system with chaotic dynamics like ours is given by the largest characteristic exponent λ_L. This number, also called the largest Liapunov exponent, provides the appropriate generalization to nonlinear systems of the familiar concept of instability exponent for a linear system (Grebogi *et al.*, 1983; Guckenheimer and Holmes, 1983, pp. 283–288; Ruelle, 1984). The values of λ_L for the trajectories of (6) are given in Table 1, for experiments 1 through 5.

The characteristic exponent increases monotonically from $\rho = \rho_1$ to $\rho = \rho_5$, in agreement with the observations about ρ-dependence of the maximum value of $C(t; p)$ made in discussing Fig. 10. The inverse λ_L^{-1} measures the average e-folding time of small errors, and decreases by a factor of 3 from $\rho = \rho_1$ to $\rho = \rho_4$ or $\rho = \rho_5$.

It is clear from Table 1, by comparing the mean e-folding time τ with the e-folding time of small errors λ_L^{-1}, that their order of magnitude, O(10 days), is the same, but their behavior is quite different: λ_L^{-1} decreases with ρ, while τ increases with ρ. Actually, τ characterizes regime predictability, as defined earlier, while λ_L^{-1} characterizes pointwise predictability, as usual. Thus their comparable magnitude is somewhat fortuitous, and probably misleading in the analysis of atmospheric data. This assertion could be tested by computing the correlation between forecast skill verified at two days or less and skill at fifteen days or more in a number of advanced numerical weather prediction models (A. Hollingsworth, personal communication, 1984). The former skill is presumably a measure of small error growth, the latter of regime predictability.

In our model, λ_L^{-1} decreases with ρ and, moreover, is larger than τ for blocked regimes, $\rho_1 \leqslant \rho \leqslant \rho_2$,

and less than τ for zonal regimes, $\rho_4 \leqslant \rho \leqslant \rho_5$. Hence, persistent sequences carry considerably increased pointwise predictability in a zonal, but not in a blocked regime, when compared to all trajectory segments of the same length in the same regime. Since λ_L^{-1} is largest in blocking regimes, $\rho_1 \leqslant \rho \leqslant \rho_2$, it follows that in such a regime, all flow patterns, not only the blocked ones, lead to pattern evolutions that are more predictable on the average than those in a zonal regime. On the other hand, the zonal regimes, $\rho_4 \leqslant \rho \leqslant \rho_5$, are characterized by a distribution of predictability properties that is very inhomogeneous in phase space, i.e., that depends very strongly on initial data. A zonal flow pattern in such a regime is much more likely to persist than a blocked pattern, while the reverse is less true in a blocking regime. Whether these results actually apply to large-scale midlatitude flows is still an open question and we shall touch upon it in the last section.

To verify the effect of numerical errors, and hence, more generally, of small modeling errors, on the persistence results discussed here, we have repeated experiment 5 with different initial data, as well as in the presence of additive random noise with a standard deviation of 10^5 times the machine accuracy, i.e., comparable to the truncation error of the scheme. The corresponding realizations of curve 5 in Fig. 17 (not shown) have the same qualitative properties, and the ordinates at each duration differ by at most 2–3% from the realization shown in Fig. 17.

The effect of pseudo-random errors in discretization is thus reproducible in our system, and one would hope the same might hold for sufficiently small modeling errors in a complex, high-resolution numerical weather prediction model (cf. Balgovind *et al.*, 1983). The numerically or randomly perturbed orbits of a dynamical system are called pseudo-orbits. We recall that when a portion of the boundary of an attractor basin of the time-continuous model system, e.g., (6), comes very close to the attractor itself, its pseudo-orbits may leave the attractor, with mean waiting times for exit depending on the size of the basin and the structure of the boundary. Moreover, for any given mean exit time, the distribution of actual waiting times may be exponential or nearly so (Grebogi *et al.*, 1983). This is in complete agreement with Fig. 17.

Hence our results suggest the following picture: for $\rho_1 \leqslant \rho \leqslant \rho_2$ there exists a single chaotic attractor, partially coexisting with the Zonal 1 stable or unstable fixed points, but lying near the Blocked, unstable fixed points. This attractor carries flows which resemble synoptically blocking patterns and are, on the average, quiescent relative to the grand-ensemble behavior of all atmospheric flows. For $\rho_4 \leqslant \rho \leqslant \rho_5$ there also exists a single, chaotic attractor, carrying flows which resemble Zonal 1 or Zonal 2 stationary solutions, and are on the average more agitated. Near $\rho = \rho_3$ a crisis occurs, the two types of chaotic attractors exchange their stability, and pseudo-orbits can switch from the neighborhood of the one to the other.

The probability of exiting from the blocking-dominated regime increases with the length of residence time (Fig. 17, curves 1 and 2). For the zonal regime, this probability decreases with residence time (Fig. 17, curves 4 and 5). In both cases, the fact that this probability is not constant, as it would be for a Markov process, suggests that the basin boundaries are rather complicated and might have fractional rather than integer dimension.

At this point we inquire whether the divergence of trajectories on the attractor is approximately constant in phase space. For this purpose, we consider the largest real part $\sigma_M(t)$ of the eigenvalues of $\mathcal{L}(t)$, where $\mathcal{L}$ is given by Eq. (10) as the instantaneous linearization of the equations of motion about a time-dependent solution $\Psi(t)$, rather than a stationary solution Ψ_s. Thus σ_M is a local rather than global measure of the divergence of trajectories, while the average $\bar{\sigma}_M$ of $\sigma_M(t)$ over a trajectory is at least λ_L. The fact that $\bar{\sigma}_M \geqslant \lambda_L$, rather than $\bar{\sigma}_M = \lambda_L$, is due to the solution of the perturbation equations $\chi(t)$ not being aligned at each point $\Psi(t)$ with the eigenvector of $\mathcal{L}(t)$ which corresponds to $\sigma_M(t)$, so that $\chi(t)$ grows at most as fast as this eigenvector.

In Figs. 18a, b, $\sigma_M(t)$ is plotted for experiments 2 and 4, respectively. It shows large variations over short time intervals when compared with other functionals of the flow field $\Psi(t; \rho)$ for the same values of the parameter ρ (compare Figs. 10b, d and 13a, c, respectively). This large variability is due at least in part to the contribution to σ_M of rapidly varying, small-amplitude fluctuations in the spatially smallest scales of motion. Such fluctuations do not appear in $C(t)$, $D_k(t)$ or other "smooth" functionals, due to the small total energy of the small scales. Another part of the fluctuations in $\sigma_M(t)$ might be due to the high sensitivity of eigenvalues to small changes in the matrix, a sensitivity which increases with the order of the eigenvalue.

The average value $\bar{\sigma}$ of $\sigma_M(t)$ is approximately 0.07 day^{-1} for $\rho = \rho_2$ and 0.11 day^{-1} for $\rho = \rho_4$. In either case, λ_L is smaller than $\bar{\sigma}$, but of the same order. Occasionally, values of $\sigma_M(t)$ as large as 0.26 and 0.47 day^{-1}, respectively, obtain.

Negative values of $\sigma_M(t)$ obtain also, indicating that at such times all eigenvalues of $\mathcal{L}(t)$ are in the left-half plane, and the trajectory $\Psi(t)$ at such points in phase space is attracting in all directions. Comparison of Figs. 18a and 10b shows that negative values of $\sigma_M(t)$ precede quite systematically minima of $C(t)$, and large values of σ_M precede maxima of C. This lagged correlation between $\sigma_M(t)$ and $C(t)$ only exists

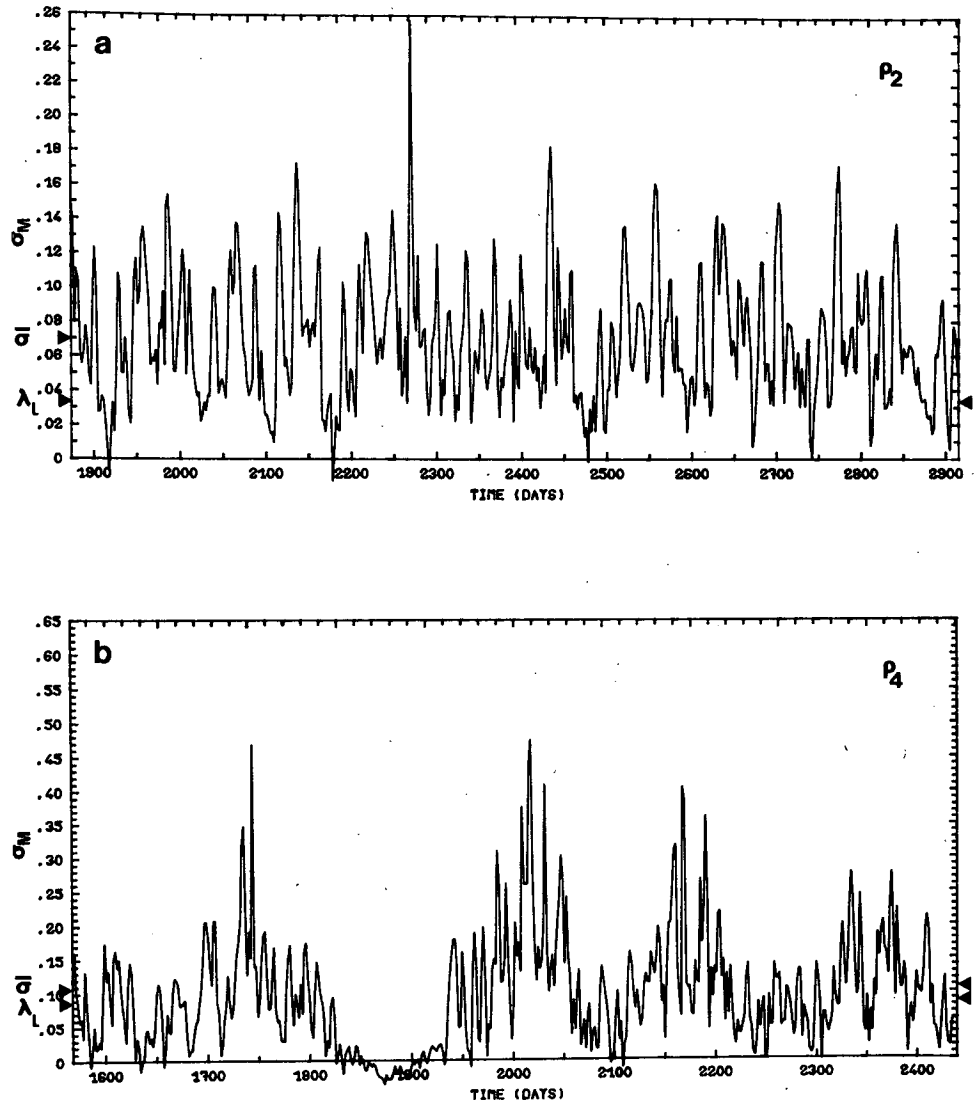

FIG. 18. Variations in time of the local rate of divergence of trajectories σ_M in experiments 2 (a) and 4 (b). Units of days^{-1} on the ordinate. The average value $\bar{\sigma}$ of σ_M over the time interval shown in the figure, and the Liapunov exponent λ_L for the extended experiment are indicated on the ordinate.

at the onset of persistent or rapidly varying sequences; otherwise one type of sequence does not differ significantly in mean divergence rate from the other.

These observations confirm the previous picture of the relation between chaotic attractors and nearby unstable fixed points, as well as the discussion in Section 5a. Persistences are associated with gradual capture of the trajectory into a contracting phase-flow region near the stable manifold of the fixed point, and rapid transients with strong instabilities along the latter's unstable manifold. This interpretation is consistent with the inverted saw-tooth aspect of all curves which plot distance between a time-dependent solution and unstable equilibria nearby (Figs. 9, 13, 16) or quantities correlated positively with such a distance (Fig. 10): rapid growth of the distance occurs along the unstable manifold of the stationary solution in question; slow decrease occurs as the unstable equilibrium is approached again along its stable manifold.

The role of phase-space localized instabilities in global transitions also helps explain the relative success of Frederiksen (1983) in obtaining blocked as well as cyclonic patterns as instabilities on suitably chosen mean flows. The point is that in the present approach the mean flows choose themselves, together with the corresponding stable and unstable wave components.

The phenomenon of approach to and quiescent

behavior near a stable or otherwise slow manifold appears even more clearly in experiment 4, where the total correlation between $\sigma_M(t)$ (Fig. 18b) and $C(t)$ (Fig. 10d) is much larger. Here the minima of $\sigma_M(t)$ are all associated with those of $C(t)$, previously identified as persistent zonal sequences, and large divergence rates occur throughout the transient episodes. Hence the contracting properties near the slow-manifold "ghost" of a Zonal 1 fixed point appear to be even more efficient at times than for the actual stable manifold of the Blocked fixed point in experiment 2. This agrees with the funneling mechanism suggested in Section 5a. In LG2 this mechanism already led to recurring sequences of zonal flow as long as 525 simulated days (Fig. 12 of LG2) for $L_R = \infty$.

Finally, it is interesting to mention another aspect of predictability associated with time intervals of rapid evolution. During such intervals, we have observed in all our experiments some reproducible sequences of events. These events are quite easily recognized by visual inspection of the time series of streamfunction fields. The identifiable events occur in the same sequence within each episode, but they do not last the same amount of time from one case to the other. This variation in relative duration makes such a recurrent sequence difficult to analyze by any known objective methods.

These results suggest the following interpretation: trajectories tend to visit certain portions of the attractor in a preferred order but dwell for variable intervals of time in each. One could thus distinguish between pattern predictability and phase predictability.

The situation is somewhat similar to numerical forecasting of frontal passages. The spatial structure of fully-developed, mature cyclone waves and associated warm and cold fronts is relatively well understood, and hence the sequence of temperature changes and precipitation events at a given location along the trajectory of the traveling disturbance is predictable with high confidence. The exact time of occurrence of each event at the given location is, however, more difficult to determine.

The only distinction is that while a synoptic-scale sequence might last 24–72 h, the planetary-scale rapid-evolution sequences discussed here can last as long as 20 days. It is still possible, however, to apply to the analysis of our global sequences the techniques used by Reed and Recker (1971) in the study of easterly waves in the equatorial Pacific, i.e., compositing observed sequences according to the phenomenological "phase" of the event in the sequence rather than according to elapsed time into the sequence.

6. Summary and discussion

We have shown that a nonlinear barotropic model of the atmosphere, spectrally truncated to 25 spherical harmonics, possesses a large variety of behavior patterns, according to the values of the forcing and dissipation parameters. Wave–wave interactions among the nonzonal modes were shown to destabilize the stationary solutions previously obtained in quasi-linear models, and lead to the existence of additional solutions, both stationary and nonstationary. Realistic-looking *blocked* and *zonal* flow patterns are obtained as coexisting, unstable stationary solutions. The synoptic realism of the blocked and zonal stationary solutions might be due to the predominantly barotropic nature of low-frequency variability in the atmosphere.

Recurrent, persistent sequences, zonal or blocked, are observed near the corresponding unstable stationary solutions in time-dependent integrations of the model. The persistence properties of solutions depend on the intensity of the forcing and on the Rossby radius of deformation. There is a demarcation in parameter space between a region where zonal flow is more persistent and one where blocked flow is more persistent. In either case, there appears to be *no preferred time scale of persistence;* the number of episodes of blocked or zonal flow of given duration decreases monotonically with the duration.

One can imagine that the forcing and dissipation in this barotropic model represent certain types of boundary conditions for the midlatitude baroclinic atmosphere. These conditions, such as equatorial sea surface temperature and pressure anomalies, may change from one season or year to another. As a result, episodes of blocked or zonal flow will occur predominantly at middle and high latitudes during the corresponding period, while transitions on shorter time scales between the two types of flow can still take place.

Such transitions are called *breaks* of a persistent pattern in classical, synoptic-statistical long-range forecasting (LRF). The timing of their occurrence is one of the major questions of LRF (Namias, 1982). Our results indicate that there are two types of causes for breaks—external and internal.

External causes such as sea surface temperature anomalies (SSTAs), snow-cover anomalies or soil-moisture anomalies will set up a certain regime that dominates over another one. In our model, they may correspond, for example, to a selection of the value of the forcing parameter ρ. For ρ small, the model possesses a single chaotic attractor, which carries predominantly blocked, quiescent flows. For ρ large, another chaotic attractor is the only one present, carrying predominantly zonal flows, which are more agitated on the average. Either attractor has a nearly constant probability of exit from the predominant regime; but this probability actually increases with length of persistent flow pattern for the blocked flows, while it decreases slightly with persistence length for zonal flows. These probabilities of exit, i.e. of breaks, can be computed from the global aspects of the

model's deterministic, nonlinear dynamics, given the known properties of numerical and modeling errors.

Internal, purely atmospheric causes for breaks have been discussed by the classical practitioners of LRF, but have not found a suitable place yet in the modern, dynamical and numerical studies of large-scale flows. The first steps in this direction are probably the articles of Egger and Schilling (1983) and of Reinhold and Pierrehumbert (1982), both of which introduce synoptic-scale waves as perturbations on the planetary-scale patterns whose persistence one wishes to forecast. These perturbations, whether deterministic or stochastic, destabilize the respective model's equilibria and lead to transitions between coexisting equilibria in finite time.

In our model, internally caused breaks correspond to the exchange of stability between two coexisting chaotic attractors, which obtain in an intermediate range of ρ values. In this range, the distribution of duration of persistent sequences results from a superposition of exit time distributions from either the zonal or the blocked attractor. An equivalent situation can arise if two concentrations of invariant measure occur on a single attractor, separated by a region of low measure density.

When interpreting these results for LRF, it is important to realize that boundary conditions may also change slowly due to atmospheric effects and other processes. Thus the distribution of exit times from a flow regime (i.e., of breaks) should not be considered as fixed on the slow time scale of a month or a season, but rather as slowly changing itself, due to atmosphere–biosphere–cryosphere–hydrosphere interactions (Ghil *et al.*, 1984).

To be more specific, we compare our results with certain observed characteristics of Northern Hemisphere atmospheric flow patterns over the Pacific and Atlantic Oceans. This separate comparison is legitimate when considering the localizing effects of relatively high boundary-layer friction on large-scale flow, which produce distinct wave trains behind major orographic features, namely the Himalayas and the Rockies, rather than a zonally-periodic flow (Held, 1983; Kalnay-Rivas and Merkine, 1981). With such an interpretation, our model suggests that the Atlantic is, climatologically, in a blocking-dominated regime, since Dole and Gordon (1983) find that over the Atlantic, blocking episodes of a certain length outnumber zonal-flow episodes of equal length. Over the northeastern Pacific, the observed situation is reversed, longer zonal episodes being more likely. The latter fact has not received much notice, since the history of the subject (see Section 1) made practitioners expect mean zonal flow at all times.

Our results indicate that persistent zonal sequences are *a priori* neither more nor less likely than persistent sequences of blocking. Which ones occur more frequently depends simply on the boundary conditions. These boundary conditions change from one year to the other, most spectacularly so in the equatorial Pacific (Bjerknes, 1969; Namias, 1982; Rasmusson and Wallace, 1983). The climatologically exceptional situation there is associated with upper-ocean El Niño events (Cane, 1983).

It has often been assumed that the impact of El Niño SSTAs on midlatitude atmospheric circulation is unique and relatively straightforward. In fact, the El Niño event of 1976 was associated with the particularly long and strong blocking episode of the 1976–77 North American winter, while the 1982–83 El Niño event was associated with the exceptionally persistent and intense zonal circulation of that winter (see also discussion in LG2). More generally, the nine El Niño events during the forty-year period 1945–84 were associated with six distinct seasonally-averaged temperature patterns over the United States (D. Gilman, personal communication, 1984; Namias and Cayan, 1984).

This variability in atmospheric response to the largest known boundary forcings appears to be more easily understood with the present results in mind. Changes in boundary data only select a preferred atmospheric regime or the coexistence of two such regimes. Neither regime precludes long flow episodes of the opposite character; it only renders them more unlikely (see also White and Clark, 1975). The persistence of either atmospheric regime will in turn affect and eventually modify boundary data, thus bringing about yet another change in flow regime (McWilliams and Gent, 1978; Philander *et al.*, 1984).

We have seen that the *relative persistence* of blocked and zonal episodes in our model corresponds roughly to observations. The absolute value of these persistences is, however, too large. There are two possible causes of this excessive persistence in the model: insufficient resolution and lack of baroclinic processes. As far as the *resolution* is concerned, a number of numerical experiments were carried out by us with 100 real modes (unpublished) and by R. Benzi (personal communication, 1983) with approximately 250 modes. Our experiments kept the same truncation at total wavenumber 9, but removed the two symmetries of the flow fields with respect to the equator and to a rotation by 180° longitude. Those of Benzi used a higher truncation at wavenumber 16, no symmetries, and a rigid lid ($L_R = \infty$).

Both sets of experiments showed roughly the same flow patterns and stability properties as those reported here. Moreover, the removal of sectorial symmetry permitted the appearance of blocked patterns over one ocean, while the other ocean exhibited zonal flow, in agreement with observations and with the discussion here. Statistics of persistence were insufficient due to increased computational cost, but indicated in general shorter persistences, as expected.

In general, given a finite-dimensional dynamical

system obtained by spectral truncation from a set of partial differential equations governing fluid flow, the qualitative and quantitative behavior of such a system seems to stabilize as the number of modes N retained in the truncation increases. Theoretical upper bounds on the number N sufficient to determine the qualitative long-term behavior of the Navier-Stokes equations in two space dimensions, and in certain three-dimensional cases, are reviewed in Barenblatt *et al.* (1983, Chapters 8 and 17). Numerical results for the two-dimensional, doubly-periodic case indicate stabilization of qualitative behavior at $N \approx 50$ and of quantitative behavior, i.e., of the critical parameter values at which pitchfork and Hopf bifurcations occur, at $N \approx 100$ (Franceschini *et al.*, 1984). This order of magnitude for N is consistent with the approximate stabilization we observe at $25 \leqslant N \leqslant 250$ and with various estimates of the actual number of degrees of freedom of large-scale atmospheric flow, namely $N = O(10^2\text{–}10^3)$ (see discussion in LG2).

Baroclinic processes were explicitly included in the model of Reinhold and Pierrehumbert (1982), which was, however, more severely truncated, with only ten horizontal modes, and had zonal channel geometry. Their persistence times, like ours, were continuously distributed and had an excessively large mean value. This overestimate can be attributed to the severe truncation and constraining geometry of their model. On the other hand, they also noticed changes in the slope of the distribution of exit times, which occurred at lower persistences than ours and were associated with the distinction in mean life time between baroclinic and barotropic processes. In our case, the changes in slope might be an indication of inherent distinctions between two or more low-frequency bands of barotropic dynamics.

In the context of our discussion, baroclinic processes affect not only the stability and persistence properties of long-lived, predominantly barotropic flow patterns. Baroclinic eddies also act in the atmosphere to transmit low-level orographic and thermal forcings to the upper levels. The way this transmission occurs is interesting in its own right and may affect to some extent the equivalent-barotropic planetary flow patterns themselves, as well as their stability (Buzzi *et al.*, 1984; Itoh, 1985; Roads, 1982).

Ideally, the study of planetary flow regimes and their persistence characteristics should be pursued with models of increasing complexity, including higher spatial resolution, baroclinic processes and explicit interactions with surface processes, such as changes in vegetation cover and upper-ocean dynamics. In this pursuit, it is important to remember that the dynamic behavior of the relatively simple model presented here could only be understood by exploring a large domain of parameter space around the physically most likely parameter values. The presence of solutions with certain attracting properties for some remote parameter values has important consequences for the persistence characteristics of solutions at the parameter values of interest. Hence, such explorations can often provide more physical insight and practical results than an increasingly detailed study of atmospheric flows restricted to a narrow domain of meticulously chosen parameters.

The message is to think globally, in both physical space and phase-parameter space. This does not mean neglect of local properties, in either space, but rather the opposite: spatial localization and suitable linearization are indispensable to an adequate description of global, nonlinear dynamics. The global and local points of view complement each other and only together allow for the study of low-frequency atmospheric variability.

Acknowledgments. Both this work and its presentation have benefited from the authors' participation in two monthly literature seminars held in the Washington area. A seminar on blocking was conducted by R. S. Lindzen at NASA Goddard Laboratory for Atmospheric Sciences (GLAS) from fall 1979 until spring 1982. A second seminar, on extended-range weather prediction and climate prediction, alternating between GLAS, the NOAA National Meteorological Center and the Department of Meteorology at the University of Maryland has been conducted by one of us (M.G.), jointly with F. Baer and J. Gerrity, starting in spring 1984. Among the participants of either or both seminars, discussions with R. Dole, D. Gilman, E. Kalnay, K. Mo, J. Namias, S. Schubert and J. Shukla were especially useful, as were those with A. Arneodo, P. Coullet, I. Held, A. Mullhaupt, R. Sadourny, J. Tavantzis and J. A. Yorke. It is a pleasure to acknowledge M. Blackmon, R. Dole, P. Webster and three anonymous reviewers for a careful reading of the original manuscript and for their numerous and constructive suggestions. The research was supported by NASA under Grant NSG-5130 and by the Centre National d'Etudes Spatiales (CNES). Most computations were carried out on the CYBER 750 of CNES at Toulouse.

APPENDIX A

Asymptotic Study of Stationary Solutions

In the limit $\alpha \to \infty$, the unique stationary solution of Eq. (1) tends to ψ^* and this remains true for the truncated problem (6). For ρ large and finite α, one stationary solution of (6) is

$$\Psi = \Psi^* + \frac{1}{\rho}\phi_1,$$

where ϕ_1 satisfies to first order in $1/\rho$

$$\mathcal{L}_1\phi_1 \equiv J_T(\Psi^*, \Delta_T\phi_1) + J_T(\phi_1, \Delta_T\Psi^*) = -J_T(\Psi^*, \mu h). \tag{A1}$$

Here J_T is the truncated Jacobian and Δ_T is the truncated Laplacian of (6).

The kernel of $\mathcal{L}_1$ is composed precisely of all zonal modes (see also Appendix C). Hence (A1) defines uniquely the nonzonal part of ϕ_1, ϕ_1', which does not depend on α, and leaves undetermined the zonal part $\bar{\phi}_1$. The indeterminacy is removed by the solvability condition to second order in $1/\rho$,

$$\int_0^{2\pi}\int_{-1}^{+1} [J_T(\phi_1, \Delta_T\phi_1 + \mu + \mu h) + \alpha\Delta_T\phi_1]Y_l^0 d\mu d\phi = 0, \quad \text{(A2)}$$

which has to be satisfied for all zonal modes Y_l^0 of the truncated solution. The solution thus determined by (A1, A2) is not necessarily the unique solution of (6) in this parameter range, and in fact other solutions exist at large ρ and sufficiently small α which are well separated from Ψ^*.

For ρ tending to 0, we assume $\Psi = \Psi^* + \phi_2$. When α and h are small with respect to unity and of the same order, the nonzonal part ϕ_2' of ϕ_2 is $O(h\Psi^*)$. It is determined to leading order by the balance between the planetary advection and the orographic forcing, which we write for simplicity in continuous form as

$$\frac{\partial\phi_2'}{\partial\lambda} = \mu\frac{\partial\psi^*}{\partial\mu}\frac{\partial h}{\partial\lambda}. \quad \text{(A3)}$$

The zonal part $\bar{\phi}_2$ in this case is $O\left(\frac{h^2}{\alpha}\psi^*\right)$ and determined by

$$-\alpha\Delta_T\bar{\phi}_2 = \overline{J_T\{\phi_2', \mu h\}}, \quad \text{(A4)}$$

where the overbar indicates zonal averaging.

If α is small with respect to h, other solutions, like $\Psi \approx c(\mu + \mu h)$ appear, but the preceding one remains valid. For h still small with respect to 1, but $\alpha \gg h$, (A3) is replaced by the balance between dissipation and orographic forcing,

$$\alpha\Delta\phi_2' = \mu\frac{\partial\psi^*}{\partial\mu}\frac{\partial h}{\partial\lambda}, \quad \text{(A5)}$$

in continuous shorthand. When $\alpha \to \infty$, $\phi_2 = \bar{\phi}_2 + \phi_2' \to 0$, and we recover the statement at the beginning of this Appendix, which holds for finite ρ as well.

The stability of the solutions above depends, in the limit $\rho \to \infty$, on the eigenvalues of the operator $-\Delta_T^{-1}\mathcal{L}_1 - \alpha$, and for $\rho \to 0$ on the eigenvalues of the operator $-\Delta_T^{-1}\mathcal{L}_2 - \alpha$, with

$$\mathcal{L}_2\chi = J_T[\chi, \mu(1 + h)].$$

The eigenvalues of both $\Delta_T^{-1}\mathcal{L}_1$ and $\Delta_T^{-1}\mathcal{L}_2$ are always equal to zero or purely imaginary for $\alpha = 0$ (cf. Appendix C). It follows that, for $\alpha > 0$, all asymptotically valid stationary solutions discussed in this Appendix are stable.

APPENDIX B

Numerical Study of Stationary Solutions

The numerical methods used in integrating the evolution equation (6) were given in LG1, Section 5.1. In this Appendix, we describe therefore only the details of the continuation method (9) used to compute stationary solutions and their stability.

The *pseudo-arclength continuation* method described here is due to Keller (1978) and allows one to follow a solution (Ψ, r) of

$$\mathbf{G}(\Psi, r) = 0, \quad \text{(B1)}$$

where $\mathbf{G}$ is a continuously differentiable map, or C^1-map, from $R^n \times R$ into R^n. We suppose that a particular solution (Ψ_0, r_0) is known and we want to obtain all other solutions (Ψ, r) which are accessible by continuous variation of r. These solutions form a C^1-manifold Γ of dimension 1 in $R^n \times R$, and Γ is parameterized by a curvilinear coordinate s.

Then the problem can be written

$$\mathbf{G}_r\dot{r} + \mathbf{G}_\Psi\cdot\dot{\Psi} = 0, \quad \text{(B2a)}$$

$$\dot{r}^2 + \|\dot{\Psi}\|_2^2 = 1, \quad \text{(B2b)}$$

$$\mathbf{G}(\Psi_0, r_0) = 0, \quad \text{(B3)}$$

where

$$(\dot{\Psi}, \dot{r}) = \left(\frac{d\Psi}{ds}, \frac{dr}{ds}\right).$$

This represents a system of $(n + 1)$ differential equations (B2) for Ψ and r, with initial condition (B3). The essential feature of (B2, B3) is that the nondegenerate singularities of the $n \times n$ matrix $\mathbf{G}_\Psi$ can be treated in this formulation as regular points.

System (B2) is discretized to obtain a series of stationary solutions (Ψ_n, r_n) which approximate the manifold Γ to be explored. The algorithm is divided into two steps. The first step is a first-order forward approximation,

$$\dot{r}_n = \pm[1 + \|\mathbf{G}_\Psi^{-1}(\Psi_n, r_n)\cdot\mathbf{G}_r(\Psi_n, r_n)\|^2]^{-1/2}, \quad \text{(B4a)}$$

$$\dot{\Psi}_n = -\dot{r}_n\mathbf{G}_\Psi^{-1}(\Psi_n, r_n)\cdot\mathbf{G}_r(\Psi_n, r_n), \quad \text{(B4b)}$$

$$\chi_{n,0} = \Psi_n + \sigma\dot{\Psi}_n, \quad \text{(B5a)}$$

$$\xi_{n,0} = r_n + \sigma\dot{r}_n, \quad \text{(B5b)}$$

where σ is a step in curvilinear coordinates. The sign of $\dot{r}_n$ defines the direction of exploration on the manifold Γ; its initial choice is arbitrary. The $\mathbf{G}_\Psi$ above is assumed at first to be nonsingular and $\mathbf{G}_\Psi^{-1}$ is its inverse. We shall see that in practice no difficulty arises from this hypothesis.

The first step, if applied repeatedly by itself, would generate rapidly cumulative errors, and the approximate solution would move away from Γ. This is prevented by the use of a corrector step, which projects the approximation $(\chi_{n,0}, \xi_{n,0})$ back on Γ by using Newton's method to find a solution of (B1).

We solve the problem

$$\mathbf{G}(\Psi_{n+1}, r_{n+1}) = 0, \tag{B6a}$$

$$N(\Psi_{n+1}, r_{n+1}, \sigma) \equiv \dot{\Psi}_n^T \cdot [\Psi_{n+1} - \Psi_n] + \dot{r}_n[r_{n+1} - r_n] - \sigma = 0 \tag{B6b}$$

by a series of iterations of the form

$$\mathbf{G}_\Psi(\chi_{n,i}, \xi_{n,i})\delta\chi_{n,i} + \mathbf{G}_r(\chi_{n,i}, \xi_{n,i})\delta\xi_{n,i} = -\mathbf{G}(\chi_{n,i}, \xi_{n,i}), \tag{B7a}$$

$$\dot{\Psi}_n^T \cdot \delta\chi_{n,i} + \dot{r}_n\delta\xi_{n,i} = -N(\chi_{n,i}, \xi_{n,i}, \sigma), \tag{B7b}$$

$$\chi_{n,i+1} = \chi_{n,i} + \delta\chi_{n,i}, \tag{B8a}$$

$$\xi_{n,i+1} = \xi_{n,i} + \delta\xi_{n,i}. \tag{B8b}$$

The iterations are continued until a convergence criterion is satisfied. The criterion used was that for $i = I$, $\|\mathbf{G}(\chi_{n,I}, \xi_{n,I})\| < \epsilon$, with ϵ prescribed. The new values of (Ψ, r) on Γ are then $\Psi_{n+1} = \chi_{n,I}$ and $r_{n+1} = \xi_{n,I}$.

The constraint (B6b) requires that the projection onto Γ be orthogonal to the direction $(\dot{\Psi}, \dot{r})$. This is a crucial feature of the algorithm, which permits in effect the exploration of Γ to pass through regular turning points of $\mathbf{G}$. Figure B1 illustrates the procedure by comparison with a projection at constant r.

The crossing of a regular turning point must be identified in order to change the sign of $\dot{r}_n$ in (B4a) and to avoid a perpetual movement of the algorithm steps to and fro. This was easy to do in our study since all eigenvalues had to be computed anyway in order to study the stability of the solution. The eigenvalue computation was performed by the QR algorithm as implemented and documented in the International Mathematics and Statistics Library of scientific subroutines (IMSL package).

The required information was thus given by a change of sign of an eigenvalue. More generally, when only the number of eigenvalues with positive real part is needed, Routh's criterion (Guillemin, 1949) may be applied to see whether this number changes by one, as it does at a turning point, or by two, as it does at a Hopf bifurcation point.

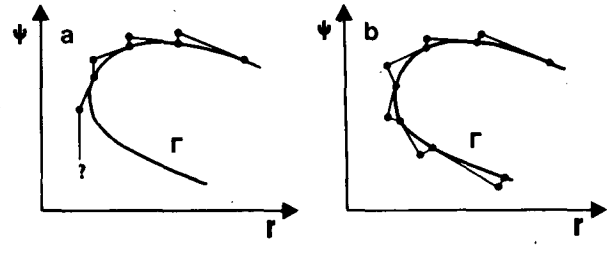

FIG. B1. Successive iterations of a continuation method (B4, 5). (a) With parallel projection only, leading to divergence of the algorithm at a turning point; (b) with a Newton correction (B6–8), equivalent to perpendicular projection from the prediction onto the solution branch.

The value of the step length σ determines the performance of the algorithm. Too small a value needlessly increases the computation time, whereas too large a value may cause divergence or a jump from one branch of solutions to another. Keller (1978) gives an estimate of σ that depends on second derivatives of $\mathbf{G}$.

We have used a single value of σ, fixed for each exploration. A set of values, suitable for all situations, has been established by trial and error. Among other possible strategies, Li and Yorke (1980) propose to control the angle between two consecutive tangent vectors on Γ limiting it to an empirically predetermined maximum and reducing σ if the limit is exceeded during one arclength step. This procedure allows simultaneous control of the crossing of regular turning points.

The application of the algorithm implies the nonsingularity of $\mathbf{G}_\Psi$, which seems to contradict the crossing of turning points. But if the turning point is nondegenerate, the probability is very small that an iteration of the algorithm fall sufficiently close to the turning point for $\mathbf{G}_\Psi$ to be numerically singular. Should this occur nonetheless, a slight modification of σ suffices, in practice, to eliminate the singularity.

It may be advantageous in order to improve the conditioning of Newton's method (B7) to replace the L_2 norm by another one in the condition (B2b). We have used in fact for the cross sections in ρ:

$$\dot{\rho}^2 + a\nabla_T\dot{\Psi} \cdot \nabla_T\dot{\Psi} = 1, \tag{B9}$$

with $a = 10$ and ∇_T the spatial gradient of the truncated field $\dot{\Psi}$. This induces a straightforward modification of the other steps, where the old norm is replaced by the new one. With this new norm, the curvature of Γ is smoother than with the L_2 norm and larger values of σ can be used.

Several variations and improvements on the method have been proposed. Li and Yorke (1980) replace the first-order forward predictor step by an explicit Runge-Kutta scheme. Glowinski (1984) replaces Newton's method by a conjugate-gradient algorithm. Kubiček and Marek (1983, p. 39) do not correct the predictor step by an orthogonal projection, but keep fixed one component of the state vector Ψ chosen by a maximum pivoting criterion.

From the point of view of further applications of this method to meteorological problems, it is important to realize that the method is in extensive routine use for the solution of nonlinear partial differential equations depending on one or more parameters in fluid dynamics, elasticity and other areas of continuum physics. Studying the stability of stationary solutions and nonlinear resonance for spatially two- and three-dimensional models of large-scale atmospheric dynamics is thus entirely feasible on currently available computers or on those expected within a decade.

It is also noteworthy from this point of view that exact Newton iteration in (B7) can be replaced by quasi-Newton (QN) iteration, i.e., the Jacobian matrices of partial derivatives $\mathbf{G}_\Psi$ and $\mathbf{G}_r$ can be replaced by partial difference matrices (Dennis and Moré, 1977; Kubiček and Marek, 1983, p. 51). The latter are much easier to program for large, three-dimensional atmospheric models such as general circulation models.

APPENDIX C

Linear Resonances for Small Topography

In the limit of vanishing topographic amplitude, $h_0 = 0$, Ψ^* is a stationary solution of (6) for all values of ρ and α. When h_0 is small enough, a perturbed solution $\Psi = \Psi^* + \phi_3$ obtains, with ϕ_3 satisfying to first order in h_0 and $\alpha = O(h_0)$

$$\mathcal{L}_3\phi_3 \equiv \rho J_T(\Psi^*, \Delta_T\phi_3) + \rho J_T(\phi_3, \Delta_T\Psi^*) + J_T(\phi_3, \mu) = -J_T(\Psi^*, \mu h). \quad \text{(C1)}$$

Equation (C1) defines the nonzonal part of ϕ_3. All zonal modes are in the nullspace of $\mathcal{L}_3$. This part of the kernel does not induce a singularity in general since the right-hand side does not possess a zonal part. However, such singularities may occur for special values of ρ, for which $\mathcal{L}_3$ also possesses a nonzonal null vector. Therefore in this Appendix we derive the solution of the zero eigenvalue problem for $\mathcal{L}_3$, concentrating on the modes with zonal wavenumber $m = 2$, which contain the orography and the right-hand side of (C1).

From the definition (5b), we have $\psi^* = -\kappa\mu^3$ with $\kappa = 0.2598$. Two useful relations are then

$$\Delta\mu^3 = 6\mu(1 - 2\mu^2) \quad \text{(C2)}$$

and the three-term recursion property (see also Balgovind *et al.*, 1983)

$$\mu^2 P_l^m(\mu) = a_l^m P_l^m(\mu) + b_l^m P_{l+2}^m(\mu) + c_l^m P_{l-2}^m(\mu), \quad \text{(C3a)}$$

with

$$a_l^m = \frac{2l^2 - 2m^2 + 2l - 1}{(2l - 1)(2l + 3)}, \quad \text{(C3b)}$$

$$b_l^m = \frac{(2l + 1)^{1/2}}{(2l + 5)^{1/2}} \frac{[(l + 1)^2 - m^2]^{1/2}[(l + 2)^2 - m^2]^{1/2}}{4(l + 1)^2 - 1}, \quad \text{(C3c)}$$

$$c_l^m = b_{l-2}^m. \quad \text{(C3d)}$$

With (C2) and (C3), one obtains

$$\mathcal{L}_3 Y_l^m = \mathrm{i}m\kappa\rho[(X + \tilde{a}_l^m)Y_l^m + \tilde{b}_l^m Y_{l+2}^m + \tilde{c}_l^m Y_{l-2}^m], \quad \text{(C4a)}$$

using the auxiliary variables $X = (1 - 6\kappa\rho)/\kappa\rho$, $d_l = 36 - 3l(l + 1)$ and

$$\{\tilde{a}_l^m, \tilde{b}_l^m, \tilde{c}_l^m\} = d_l\{a_l^m, b_l^m, c_l^m\}. \quad \text{(C4b)}$$

For a given zonal wavenumber m, the matrix A of $-i\mathcal{L}_3/m\rho\kappa$ is tridiagonal, since only odd values of l are present, and has real coefficients. The resonances of $\mathcal{L}_3$ are given by the values of X which cancel the determinant of A. Moreover, A is of the form $\mathsf{A} = XI - \tilde{\mathsf{A}}$; the problem thus reduces to finding the eigenvalues X of a tridiagonal real matrix $\tilde{\mathsf{A}}$.

Since the entries of $\tilde{\mathsf{A}}$ are nonnegative, the largest eigenvalue in absolute value is necessarily real and positive. Moreover, $\tilde{\mathsf{A}}$ is diagonally dominant,

$$|\tilde{a}_l^m| \geq |\tilde{b}_l^m| + |\tilde{c}_l^m|,$$

so that its eigenvalues have the same sign as those of its diagonal entries, $-\tilde{a}_l^m$, i.e., nonnegative.

For $m = 2$ and the truncation scheme shown in Fig. 1, we have

$$-\tilde{\mathsf{A}} = \begin{bmatrix} \tilde{a}_3^2 & \tilde{b}_3^2 & 0 & 0 \\ \tilde{c}_5^2 & \tilde{a}_5^2 & \tilde{b}_5^2 & 0 \\ 0 & \tilde{c}_7^2 & \tilde{a}_7^2 & \tilde{b}_7^2 \\ 0 & 0 & \tilde{c}_9^2 & \tilde{a}_9^2 \end{bmatrix}. \quad \text{(C5)}$$

Since $\tilde{a}_3^2 = \tilde{b}_3^2 = \tilde{c}_5^2 = 0$, $X_0 = 0$ is an eigenvalue of $\tilde{\mathsf{A}}$. The three other solutions of the characteristic equation for $\tilde{\mathsf{A}}$ are $X_1 = 12.08$, $X_2 = 48.75$ and $X_3 = 136.3$, so that all eigenvalues are indeed real and nonnegative.

These values of X lead respectively to the linearly resonant parameter values $\rho_0^R \approx 0.6145$, $\rho_1^R \approx 0.2129$, $\rho_2^R \approx 0.07030$ and $\rho_3^R \approx 0.02705$, which are indicated on the abscissa in Fig. 4. They initiate clearly the nonlinear resonances apparent in the figure at finite values of h_0.

As a by-product of this analysis, we can also derive properties of the operator $\Delta_T^{-1}\mathcal{L}_1$ defined in Appendix A, since $\mathcal{L}_1$ and $\mathcal{L}_3$ differ only by a diagonal term. Each m-block of the matrix $-\Delta_T^{-1}\mathcal{L}_1$ has the same structure as that of $-i\mathcal{L}_3/m\kappa\rho$.

From this we deduce immediately that all eigenvalues of $\Delta_T^{-1}\mathcal{L}_1$ corresponding to zonal modes are zero, while they are purely imaginary and nonzero for nonzonal modes. For $m = 2$, the eigenvalues are respectively $\sigma_0 = \pm 12i$, $\sigma_1 = \pm 36.6i$, $\sigma_2 = \pm 109.5i$ and $\sigma_3 = \pm 284.6i$, conjugate values appearing when one considers $\mathcal{L}_1 Y_l^m$ and $\mathcal{L}_1 Y_l^{-m}$.

The results above allow us to explore the behavior of resonances when one extends the truncation in total wavenumber l at a given zonal wavenumber m. We preserve here the same symmetries as in the basic truncation scheme and thus consider only odd values of l.

Let A_L be the matrix associated with the truncation at $l = L$. We have the following recursion relation for its determinant D_L:

$$D_L = (\tilde{a}_L^m + X)D_{L-2} - \tilde{b}_L^m \tilde{c}_L^m D_{L-4}.$$

It is more convenient at this point to return to the matrix A'_L with entries (C3b–d), yielding the recursion

$$E_L = (a_L^m + X/d_L)E_{L-2} - b_{L-2}^m c_L^m E_{L-4}, \quad \text{(C6a)}$$

where E_L is the determinant of $\mathbf{A}'_L$ and

$$a_L^m = \frac{1}{2} + \frac{1}{8L^2}(1 - 4m^2) + O(L^{-3}), \quad \text{(C6b)}$$

$$b_{L-2}^m = c_L^m = \frac{1}{4} - \frac{1}{16L^2}(1 + 4m^2) + O(L^{-3}). \quad \text{(C6c,d)}$$

To simplify notation, we consider the recursion

$$P_n(x) = (a_n - b_n x)P_{n-1}(x) - c_n P_{n-2}(x), \quad \text{(C7a)}$$

where $n = L$, the superscript m has been omitted, $x = X(\rho)$, and

$$a_n = a_0 + O(n^{-2}), \quad b_n = O(n^{-2}), \quad c = c_0 + O(n^{-2}), \quad \text{(C7b,c,d)}$$

with $a_0 = 1/2 > c_0 = 1/16 > 0$ and $b_n > 0$.

Intuitively, as $n \to \infty$, $b_n \to 0$ and the leading term of $P_n(x)$ will behave like $(\Pi_0^n b_k)x^n$, so that one root of P_n, call it X_n, will have to become very large, $X_n \to \infty$. More precisely, let us assume that the roots $x_k(n)$ of $P_n(x)$, $0 \leq n \leq N-1$, lie between 0 and X_{N-1}, $0 \leq x_k^{(n)} \leq X_{N-1}$, with $X_n = x_n^{(n)}$. Then (C7) implies that

$$X_N = \frac{a_N}{b_N} - \frac{c_N P_{N-2}(X_N)}{b_N P_{N-1}(X_N)} \equiv f_N(X_N). \quad \text{(C8)}$$

For large x, the second term in $f_N(x)$ behaves like $-c_N/(b_N x)$, since b_{N-2}/b_{N-1} is bounded. Thus the iterative solution $x^{(i)} = f_N[x^{(i-1)}]$ of (C8), with $x^{(0)}$ sufficiently large, will converge to the leading root $x_N^{(N)} = X_N$ of $P_N(x)$ and

$$X_N = \frac{a_N}{b_N} + O(1) = O(N^2). \quad \text{(C9)}$$

It is obvious that $X_N > 0$ and easy to verify that $X_N > X_{N-1}$ for N large enough.

It is true, but somewhat harder to prove, that *all* zeros of $P_n(x)$ tend to an asymptotic distribution with only finitely many zeros in any finite interval. The technical tools required appear in Beraha *et al.* (1978) and references therein.

Recall that $x \to \infty$ is equivalent to $\rho \to 0$. Thus the linear resonances for small h_0 and α, studied here, accumulate near $\rho = 0$ as the number of meridional modes increases. A related mechanism might be at work in creating the multiple folds of the second nonlinear resonance observed numerically for finite h_0, ρ and α, especially as $\alpha \to 0$ (curve I, Fig. 3e, $\alpha = 0.033$), but the analysis is more difficult and the relevant stationary solution is more complicated than Ψ^*.

An excellent analysis of the continuous problem on an equatorial β-plane was outlined by one of the referees. We hope that it will be fully worked out and published independently. As indicated in Section 6, the behavior of truncated models as the number of modes retained in the truncation increases is a topic of active research, which is certainly of great interest in the present context.

REFERENCES

Arneodo, A., P. Coullet and C. Tresser, 1982: Oscillators with chaotic behavior: An illustration of a theorem by Shil'nikov. *J. Stat. Phys.*, **27**, 171–182.

Arnold, V. I., 1978: *Ordinary Differential Equations*, 2nd ed. MIT Press, 280 pp.

——, 1983: *Geometrical Methods in the Theory of Ordinary Differential Equations*. Springer-Verlag, 334 pp.

Balgovind, R., A. Dalcher, M. Ghil and E. Kalnay, 1983: A stochastic-dynamic model for the spatial structure of forecast error statistics. *Mon. Wea. Rev.*, **111**, 701–722.

Barenblatt, G. I., G. Iooss and D. D. Joseph (Eds.), 1983: *Nonlinear Dynamics and Turbulence*. Pitman, 356 pp.

Beraha, S., J. Kahane and N. J. Weiss, 1978: Limits of zeros of recursively defined families of polynomials. *Studies in Foundations and Combinatorics, Adv. Math. Suppl. Studies*, Vol. I, G.-C. Rota, Ed., 213–232.

Bjerknes, J., 1969: Atmospheric teleconnections from the equatorial Pacific. *Mon. Wea. Rev.*, **97**, 163–172.

Blackmon, M., R. A. Madden, J. M. Wallace and D. S. Gutzler, 1979: Geographical variations in the vertical structure of geopotential height fluctuations. *J. Atmos. Sci.*, **36**, 2450–2466.

Burridge, D. M., and E. Källén (Eds.), 1984: *Problems and Prospects in Long and Medium Range Weather Forecasting*. Springer-Verlag, 274 pp.

Buzzi, A., A. Trevisan and A. Speranza, 1984: Instabilities of a baroclinic flow related to topographic forcing. *J. Atmos. Sci.*, **41**, 637–650.

Cane, M., 1983: Oceanographic events during El Niño. *Science*, **222**, 1189–1195.

Charney, J. G., 1947: The dynamics of long waves in a baroclinic westerly current. *J. Meteor.*, **4**, 135–163.

——, 1973: Planetary fluid dynamics. *Dynamic Meteorology*, P. Morel, Ed., Reidel, 97–351.

——, and J. G. DeVore, 1979: Multiple flow equilibria in the atmosphere and blocking. *J. Atmos. Sci.*, **36**, 1205–1216.

Cotter, C. H., 1966: *The Astronomical and Mathematical Foundations of Geography*. American Elsevier, 244 pp.

Davey, M., 1981: A quasi-linear theory for rotating flow over topography. Part II: β-plane annulus. *J. Fluid Mech.*, **99**, 267–292.

Dennis, J. E., and J. J. Moré, 1977: Quasi-Newton methods, motivation and theory. *SIAM Review*, **19**, 46–89.

Dole, R. M., and N. D. Gordon, 1983: Persistent anomalies of the extratropical Northern Hemisphere wintertime circulation: Geographical distribution and regional persistence characteristics. *Mon. Wea. Rev.*, **111**, 1567–1586.

Eady, E. T., 1949: Long waves and cyclone waves. *Tellus*, **1**, 33–52.

Egger, J., 1978: Dynamics of blocking highs. *J. Atmos. Sci.*, **35**, 1788–1801.

——, and H.-D. Schilling, 1983: On the theory of the long-term variability of the atmosphere. *J. Atmos. Sci.*, **40**, 1073–1085.

Feigenbaum, M. J., 1978: Quantitative universality for a class of nonlinear transformations. *J. Stat. Phys.*, **19**, 25–52.

Franceschini, V., C. Tebaldi and F. Zironi, 1984: Fixed point limit behavior of N-mode truncated Navier-Stokes equations as N increases. *J. Stat. Phys.*, **35**, 387–397.

Frederiksen, J. S., 1983: A unified three-dimensional instability theory of the onset of blocking and cyclogenesis. Part II: Teleconnection patterns. *J. Atmos. Sci.*, **40**, 2593–2609.

Gaspard, P., and G. Nicolis, 1983: What can we learn from

homoclinic orbits in chaotic dynamics? *J. Stat. Phys.*, **31**, 499–518.

Ghil, M., 1976: Climate stability for a Sellers-type model. *J. Atmos. Sci.*, **33**, 3–20.

——, and J. Tavantzis, 1983: Global Hopf bifurcation in a simple climate model. *SIAM J. Appl. Math.*, **43**, 1019–1041.

——, R. Benzi and G. Parisi (Eds.), 1984: *Turbulence and Predictability in Geophysical Fluid Dynamics and Climate Dynamics.* North-Holland, Amsterdam, 347–402.

Glowinski, R., 1984: *Numerical Methods for Nonlinear Variational Problems.* Springer-Verlag, 204.

Grebogi, C., E. Ott and J. A. Yorke, 1983: Crises, sudden changes in chaotic attractors, and transient chaos. *Physica 7D*, 181–200.

Guckenheimer, J., and P. Holmes, 1983: *Nonlinear Oscillations, Dynamical Systems, and Bifurcations of Vector Fields.* Springer-Verlag, 453 pp.

Guillemin, E., 1949: *The Mathematics of Circuit Analysis,* Wiley, 395.

Held, I. M., 1983: Stationary and quasi-stationary eddies in the extratropical troposphere: Theory. *Large-Scale Dynamic Processes in the Atmosphere,* B. J. Hoskins and R. P. Pearce, Eds., Academic Press, 127–168.

Hide, R., N. T. Birch, L. V. Morrison, D. J. Shea and A. A. White, 1980: Atmospheric angular momentum fluctuations and changes in the length of day. *Nature,* **286**, 114–117.

Hoskins, B., and D. J. Karoly, 1981: The steady linear response of a spherical atmosphere to thermal and orographic forcing. *J. Atmos. Sci.*, **38**, 1179–1196.

Itoh, H., 1985: The formation of quasi-stationary waves from a viewpoint of bifurcation theory. *J. Atmos. Sci.*, in press.

Kadanoff, L. P., 1983: Roads to chaos. *Physics Today,* Dec. issue, 46–53.

Kalnay-Rivas, E., and L.-O. Merkine, 1981: A simple mechanism for blocking. *J. Atmos. Sci.*, **38**, 2077–2091.

Källén, E., 1984: Bifurcation mechanisms and atmospheric blocking. *Problems and Prospects in Long and Medium Range Weather Forecasting,* D. M. Burridge and E. Källén, Eds., Springer-Verlag, 229–263.

Keller, H. B., 1978: Global homotopies and Newton methods. *Nonlinear Analysis,* C. de Boor and G. H. Golub, Eds., Academic Press, 73–94.

Krishnamurti, T. N., and Subrahmanyan, D., 1982: The 30–50 day mode at 850 mb during MONEX. *J. Atmos. Sci.*, **39**, 2088–2095.

Kubiček, M., and M. Marek, 1983: *Computational Methods in Bifurcation Theory and Dissipative Structures.* Springer-Verlag, 243 pp.

Legras, B., and M. Ghil, 1983: Ecoulements atmosphériques stationnaires, périodiques et apériodiques. *J Méc. Théor. Appl.*, No. spécial 1983, 45–82.

——, and ——, 1984: Blocking and variations in atmospheric predictability. *Predictability of Fluid Motions,* G. Holloway and B. J. West, Eds., American Institute of Physics, 87–105.

Leith, C. E., 1984: Dynamically stable nonlinear structures. *Problems and Prospects in Long and Medium Range Weather Forecasting,* D. M. Burridge and E. Källén, Eds., Springer-Verlag, 265–274.

Li, T. Y., and J. A. Yorke, 1980: A simple reliable numerical algorithm for following homotopy paths. *Analysis and Computation of Fixed Points,* M. Robinson, Ed., Academic Press.

Lorenz, E. N., 1963: Deterministic nonperiodic flow. *J. Atmos. Sci.*, **20**, 130–141.

——, 1967: *The Nature and Theory of the General Circulation of the Atmosphere.* World Meteorological Organization, 161 pp.

——, 1984: The growth of errors in prediction. *Turbulence and Predictability in Geophysical Fluid Dynamics and Climate Dynamics,* M. Ghil and Co-Editors, 243–265.

Madden, R. A., and P. R. Julian, 1971: Detection of a 40–50 day oscillation in the zonal wind in the Tropical Pacific. *J. Atmos. Sci.*, **28**, 702–708.

Malanotte-Rizzoli, P., 1982: Planetary solitary waves in geophysical flows. *Adv. Geophys.*, **24**, 147–224.

McWilliams, J. C., 1980: An application of equivalent modons to atmospheric blocking. *Dyn. Atmos. Oceans,* **5**, 43–66.

——, and P. R. Gent, 1978: A coupled air and sea model for the tropical Pacific. *J. Atmos. Sci.*, **35**, 982–989; Corrigendum *J. Atmos. Sci.*, **36**, 181.

Namias, J., 1950: The index cycle and its role in the general circulation. *J. Meteorol.*, **7**, 130–139.

——, 1982: *Short Period Climatic Variations, Collected Works of J. Namias.* 3 vols. (1934–1982), University of California, San Diego.

——, and D. Cayan, 1984: El Niño—Implications for forecasting. *Oceanus,* **27**(2), 40–45.

Pedlosky, J., 1979: *Geophysical Fluid Dynamics.* Springer-Verlag, 624 pp.

——, 1981: Resonant topographic waves in barotropic and baroclinic flows. *J. Atmos. Sci.*, **38**, 2626–2641.

Philander, S. G. H., T. Yamagata and R. C. Pacanowski, 1984: Unstable air–sea interactions in the tropics. *J. Atmos. Sci.*, **41**, 604–613.

Pierrehumbert, R. T., and P. Malguzzi, 1984: Forced coherent structures and local multiple equilibria in a barotropic atmosphere. *J. Atmos. Sci.*, **41**, 246–257.

Rasmusson, E. M., and J. M. Wallace, 1983: Meteorological aspects of the El Niño/Southern Oscillation. *Science,* **222**, 1195–1202.

Reed, R. J., and E. E. Recker, 1971: Structure and properties of synoptic-scale wave disturbances in the equatorial Western Pacific. *J. Atmos. Sci.*, **28**, 1117–1133.

Reinhold, B. B., and R. T. Pierrehumbert, 1982: Dynamics of weather regimes: Quasi-stationary waves and blocking. *Mon. Wea. Rev.*, **110**, 1105–1145.

Rex, D. F., 1950a: Blocking action in the middle troposphere and its effect on regional climate. Part I: An aerological study of blocking action. *Tellus,* **2**, 196–211.

——, 1950b: Part II: The climatology of blocking action. *Tellus,* **2**, 275–301.

Roads, J. O., 1982: Stable and unstable near-resonant states in multi-level, severely truncated, quasi-geostrophic models. *J. Atmos. Sci.*, **39**, 203–224.

Rossby, C.-G., 1939: Relations between variations in the intensity of the zonal circulation and the displacements of the semi-permanent centers of action. *J. Mar. Res.*, **2**, 38–55.

Ruelle, D., 1984: The onset of turbulence, a mathematical introduction. *Turbulence and Predictability in Geophysical Fluid Dynamics and Climate Dynamics,* M. Ghil and Co-Editors, 3–16.

Shilnikov, L. P., 1965: A case of the existence of a denumerable set of periodic motions. *Sov. Math. Dokl.*, **6**, 163–166.

Shukla, J., and K. C. Mo, 1983: Seasonal and geographic variations of blocking. *Mon. Wea. Rev.*, **111**, 388–402.

Sumner, E. J., 1954: A study of blocking in the Atlantic–European sector of the Northern Hemisphere. *Quart. J. Roy. Meteor. Soc.*, **80**, 402–416.

Tung, K. K., and R. S. Lindzen, 1979: A theory of stationary long waves. Part I: A simple theory of blocking. *Mon. Wea. Rev.*, **107**, 714–734.

White, W. B., and N. E. Clark, 1975: On the development of blocking ridge activity over the central North Pacific. *J. Atmos. Sci.*, **32**, 489–502.